J. Fluid Mech. (1981), *vol.* 112, *pp.* 33–70
Printed in Great Britain

A structural model for turbulent exchange in boundary layers

By A. C. M. BELJAARS†, K. KRISHNA PRASAD AND D. A. DE VRIES

Laboratory for Fluid Dynamics and Heat Transfer, University of Technology, Eindhoven, Netherlands

(Received 14 December 1979 and in revised form 14 November 1980)

In this paper a model is presented that incorporates characteristic features of the turbulent structures as revealed by recent experimental observations. The principal characteristic features are the occurrence of periodicity and intermittency, not only at the edge of the boundary layer, but also close to the wall.

By an averaging procedure, equations are derived for the large-scale part of the turbulent motion. The unknown terms, representing the small-scale turbulent stress, are assumed to be zero except in the so-called burst regions which occupy only a small fraction of the total flow field and arise from local instability of the large-scale flow field. In the model distinction is made between a thin layer near the wall where viscous forces play an important role and the remaining part of the boundary layer where inviscid equations are valid. The momentum transport takes place in three different stages with different mechanisms. First of all the fluid in the wall region is retarded by viscous forces and collected in long narrow regions (streaks). After this a rapid exchange takes place in the burst regions where the low-momentum fluid is ejected into the outer region. Finally the large-scale structures in the outer region take over the transport.

It turns out that the transport properties of a turbulent boundary layer can be calculated reasonably well with this deterministic model. It can be concluded that the coherent part of the turbulent motion is very important in the transport process.

1. Introduction

It is becoming increasingly evident that many turbulent flows are less chaotic than one is led to believe from a cursory examination of hot-wire traces obtained from different laboratory flows. Visual studies in shear layers and wall-bounded flows have established that there exist definitely recognizable flow patterns which not only persist for long periods of time in the dominant flow direction, but also are constantly generated anew at time intervals that fluctuate around a well-defined mean. Understanding of these flow patterns – often called 'coherent structures' or simply 'structures' – has been greatly enhanced by quantitative experimental information that has been gathered especially through the use of the recently developed technique of conditional sampling. In particular these structures have been held to be responsible for substantial contributions to the Reynolds stress and therefore are very important in determining the transport properties of turbulence.

† Present affiliation: Royal Netherlands Meteorological Institute, De Bilt, Netherlands.

There have been several reviews published from time to time summarizing the current knowledge on these structures; perhaps the most exhaustive one is due to Willmarth (1975*a*). We shall discuss these experimental findings at greater length in the next section where we shall develop a physical model that is accessible to calculations using well-known ideas from laminar boundary-layer theory and inviscid hydrodynamics. We now turn our attention to a brief description of theoretical attempts to 'explain' the physics governing these structures.

Because of the complexities associated with the nonlinearities of the problem, most of the theoretical inquiries on the structures are confined to linear formulations of the incompressible two-dimensional boundary-layer flows. The starting point for the formulations is the decomposition of the flow field into a mean and a fluctuating part, as

$$\mathbf{u}(\mathbf{x},t) = \bar{\mathbf{u}}(\mathbf{x}) + \mathbf{u}'(\mathbf{x},t), \quad p(\mathbf{x},t) = \bar{p}(\mathbf{x}) + p'(\mathbf{x},t), \tag{1}$$

where overbars are used to indicate the mean quantities. The equations are then simplified by assuming a parallel mean flow

$$\frac{\partial \mathbf{u}'}{\partial t} + \bar{u}\frac{\partial \mathbf{u}'}{\partial x} + v'\frac{\partial \bar{u}}{\partial y}\mathbf{I} + \frac{1}{\rho}\nabla p' - \nu\nabla^2\mathbf{u}' = \frac{1}{\rho}\nabla.\tau_{\mathbf{uu}}, \quad \nabla.\mathbf{u}' = 0, \tag{2}$$

where $\tau_{\mathbf{uu}} = \rho(\overline{\mathbf{u}'\mathbf{u}'} - \mathbf{u}'\mathbf{u}')$, $\mathbf{I} = (1,0,0)$, ν is the kinematic viscosity, ρ is density, $\bar{\mathbf{u}} = (\bar{u},0,0)$ and $\mathbf{u}' = (u',v',w')$. A variety of tactics is adopted to approximate equations (2), most of which restrict attention to processes occurring in a thin layer near the wall. Detailed summaries of these linear theories are available in Hinze (1975) and Beljaars (1979); our intention here is merely to focus attention on questions that concern us in this work and hence the treatment below will be sketchy.

The simplest model, proposed independently by Einstein & Li (1956) and Hanratty (1956), reduces equations (2) to a diffusion equation. This model, often referred to as surface renewal theory, considers an intermittent layer whose growth in time by diffusion is interrupted by some kind of instability which brings the turbulent region into intimate contact with the wall, after which the layer grows again.

The mean velocity and mean shear stress averaged over one period agree very well with experimental data for a particular choice of the period, which turns out to be quite close to the interval between two successive events of intense turbulent activity in the wall region, the so-called 'bursts' (Laufer & Badri Narayanan 1971). The model, because of its simplicity and modest predictive capability, has proved very popular in diverse applications (see for example Thomas, Chung & Mahaldar 1971; Ooms *et al.* 1978). The model is, however, far too crude to serve the purposes of providing an explanation for the complex processes that take place in the wall region of a turbulent boundary layer, as will be shown later.

The second approach is to set the turbulent stress terms in (2) to zero, assume a basic mean flow $\bar{u}(y)$ and study the behaviour of $\mathbf{u}'$ in a region close to the wall subject to suitable initial and boundary conditions (Sternberg 1962; Schubert & Corcos 1967). The theory yields results which are in qualitative agreement with experiments on spectrum of u', phase relations between u' and v', etc. However it fails to predict the Reynolds stresses and moreover it assigns a rather passive role to the wall region, in contradiction to currently known experimental information.

Perhaps the most interesting theory of this kind is due to Landahl (1965, 1967),

where a second level of decomposition of the fluctuating field into a large-scale part (scaling on the boundary-layer thickness) and a small-scale part (scaling on the viscous-layer thickness) is carried out.

This procedure enables Landahl to relegate the nonlinearities to the equations of the small-scale field which in turn drives the large-scale field. Again $\overline{u}(y)$ is assumed known. Specifically, the model attempts to take into account the localized regions of bursting in the wall layer. A notable feature of the calculations performed with the model by Landahl (1967) and Bark (1975) is the success in predicting the decay of pressure fluctuations in the streamwise direction (Willmarth 1975*b*).

In a subsequent application of the above theory, Landahl (1975) provides heuristic arguments for the periodic generation of bursts. Computations carried out by one of the authors (Beljaars 1979) on the basis of the theory did not lead to any conclusive results and, moreover, led to doubts about the way in which the problem has been posed. In contrast to Landahl's assumption that bursts behave like pulses in time, it is believed that bursts are narrow regions that move downstream in a more or less frozen way. A problem with the numerical results of Landahl and Bark is that they are given in the wave-vector domain and are obtained by representing the effect of bursts in a statistical manner. The averaging involved in such a procedure obscures information about individual events. Transformation of the numerical results to the space domain only leads to correlation functions that are difficult to interpret.

A striking feature of the theories described above (apart from the rather uninteresting statement that they are only linear!) is their lack of attention to the all-important aspect of transport properties of turbulence. While the bursting phenomenon is taken into account in some of the theories, they are unable to point out mechanisms that are responsible for constant regeneration of these bursts. Moreover the active interaction that obviously exists between the inner and outer regions of a turbulent boundary layer is more or less ignored. It is to these specific questions that we address ourselves in this work. We concentrate on the individual events in the turbulent boundary layer, so much so that our approach is purely deterministic. This is not to say that statistical features do not have any role in determining the 'events' in a turbulent boundary layer, but helps us to hold the mathematical and computational tasks to tractable proportions. In particular this procedure assists in retaining the nonlinearities of the problem more or less intact.

2. The physical model

A recurrent feature throughout the present work is the distinction between two regions in the turbulent boundary layer – an inner region close to the wall characterized by the presence of viscosity and an outer region where the viscous influence can be ignored. This is supported by both experimental evidence and more general asymptotic arguments of the type provided by Mellor (1972). Before presenting the model, a brief summary of the relevant experimental results will be given below.

2.1. *The experimental evidence*

Five principal features emerge from flow visualization and conditional sampling experiments for the wall region. First, the flow-visualization studies of Kline *et al.* (1967) and Corino & Brodkey (1969) demonstrate that the wall region is characterized

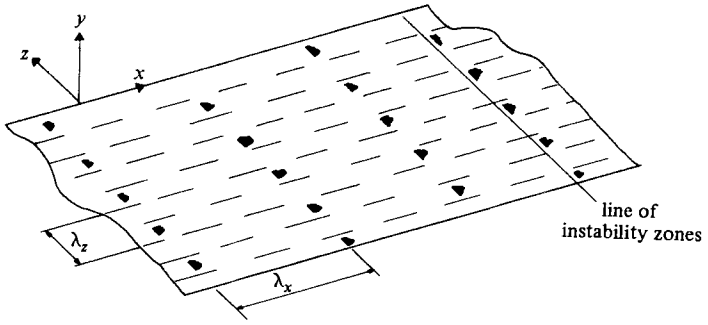

FIGURE 1. The moving instability zones in the wall layer.

by long (in the streamwise direction), narrow (in the spanwise direction) regions of relatively quiescent retarded motion punctuated by short periods of intense turbulent activity (which we call 'bursts', which may include many component events (see Kim, Kline & Reynolds 1971). Secondly, the retarded flow structure scales with the viscous-layer thickness in the spanwise direction. Thirdly, the bursting regions scale in both directions with the viscous-layer thickness. Fourthly, the bursts are responsible for removing the fluid accumulated in the retarded layer and ejecting it into the outer layer. The ejected fluid is replaced by high momentum fluid from the edge of the wall layer to maintain continuity, thus preparing the ground for the start of a fresh cycle. Lastly, the conditional averaging experiments of Blackwelder & Kaplan (1972) show an inflectional velocity profile prior to the occurrence of a burst, suggesting that bursts are initiated by some form of local instability.

Turning now to the outer region, the wavy interface between turbulent and non-turbulent fluid at the edge of the boundary layer is a clear manifestation of the presence of structures there. Blackwelder & Kovasznay (1972) suggest that large-scale vortex structures, with their axes in the spanwise direction, are responsible for the wavy interface. Correlation measurements show that these vortices keep their identity over large distances downstream. From a conditional sampling experiment, Brown & Thomas (1977) establish that these large-scale structures run in phase with the wall-layer cycle. Laufer (1972) suggests that large-scale vortices roll over the wall and induce instabilities in the wall region.

2.2. *The model*

An idealized phenomenological picture of the turbulent boundary layer will be derived now from the experimental features discussed above. There are three distinct elements in the model: (i) the wall layer; (ii) the outer region; and (iii) interactions between the two. The model represents the burst events in the wall layer by instability zones with spacing λ_x and λ_z in the x and z directions and these zones are assumed to move at a uniform velocity – the convection velocity, U_c. This results in a stationary picture for the wall layer in a co-ordinate reference frame that moves downstream with this velocity (see figure 1).

A picture similar to that in figure 1 was presented by Black (1968). Black attempts a detailed description of small-scale processes while we limit ourselves more or less exclusively to large-scale motions. In addition it appears to us that Black did not fully exploit the idea of moving burst events.

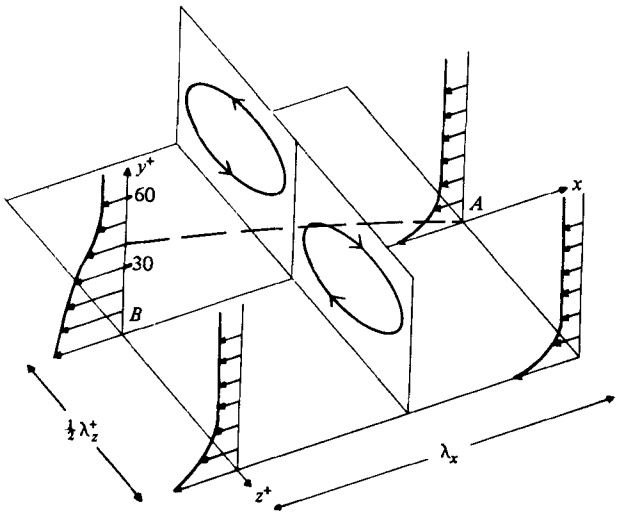

FIGURE 2. Developing wall layer between two instability zones as seen by an observer in the moving co-ordinate system.

For an observer at rest in the laboratory frame, the spatial periodicity in figure 1 appears as a periodicity in time and the small size of the instability zones shows up as an intermittency in the records obtained at a fixed point of observation. The instability zones are assumed to be responsible for the event of the removal of low-momentum fluid from the wall region; as a consequence of this, and continuity requirements, this ejected fluid is replaced by high-momentum fluid from the edge of the wall region ($y^+ \simeq 60$). This high-momentum fluid is retarded by the development of a viscous boundary layer which is terminated by a new instability zone.

The periodicity in the z direction is assumed to arise out of counter-rotating longitudinal vortices in the wall region between two lines of instability zones (cf. Blackwelder & Eckelmann 1979, for experimental support). They cause an accumulation of low-momentum fluid in streaks and give the instability zone a local character in the z direction as well. The role of these counter-rotating vortices in producing a streaky structure can be understood from the convected frame representation in figure 2. They disturb the viscous boundary layer that starts developing from A, which is assumed to coincide with a line of instability zones. At the z locations where the secondary motion is outwards a streak with wall velocity will develop (corresponding to a low-speed streak in the fixed co-ordinates); at z locations where the longitudinal vorticity produces a wallward motion, the boundary-layer development is suppressed (corresponding to high-speed streaks in the laboratory frame). Almost all the low-momentum fluid retarded by viscous forces is swept together in a low-speed streak, on top of which an inflectional velocity profile develops.

The structures in the outer region are assumed to be two-dimensional and vortex-like as indicated in figure 3. The period for these structures is taken to be λ_x as well. An individual structure in the wall region sees the structure in the outer region as essentially two-dimensional since the former has a spanwise extent of λ_z, which is an order of magnitude smaller than that for the latter ($\sim \lambda_x$). In other words one outer region structure is related to a number of wall region structures in the spanwise

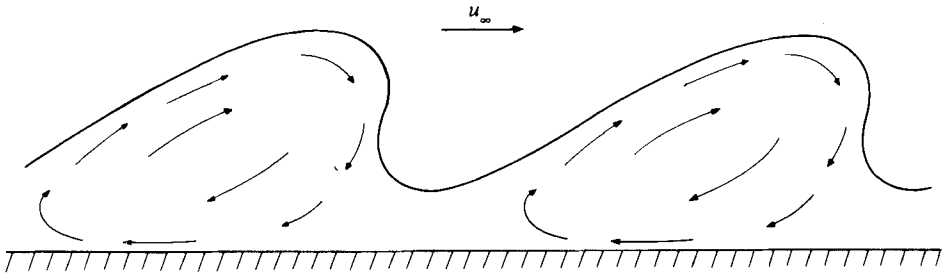

FIGURE 3. Structures in the outer region seen by an observer in the moving co-ordinate system.

direction. Thus the two-dimensional assumption can be expected to represent the interaction between the outer and wall-region structures reasonably well in an overall sense.

However, the situation is not as clear with respect to momentum transport in the outer layer. The conceptual picture of figure 3 has been drawn by many other investigators (cf. Brown & Thomas 1977; Falco 1977; Kovasznay, Kibens & Blackwelder 1970; Laufer 1972). Most of the investigators suggest that these motions are three-dimensional. However, the available experimental evidence does not clarify whether these three-dimensional motions are essential for the transport of momentum.

Under these circumstances it appears expedient to adopt a two-dimensional model for the outer structures, at least for the sake of holding the computational effort to modest proportions. Thus the present model has a twofold purpose: (i) to determine by computation whether two-dimensional eddies can explain the momentum transport and boundary-layer growth; and (ii) to investigate the nature of interaction between the outer and wall layers. In the final section of the paper we shall discuss the assumption of two-dimensionality in relation to the computational results.

The assumption that the λ_x in the wall region is equal to that in the outer region appears to conflict with experimental observation (Laufer & Badri Narayanan 1971) of a difference of factor 2 between the period in the wall region and that in the outer region. This difference can be explained on the basis of the experimental results of Offen & Kline (1974, 1975). They observed that the low-speed streaks in two successive cycles are shifted over $\frac{1}{2}\lambda_z$ with respect to each other in the z direction. The situation is illustrated schematically in figure 4. Because of this shift, to an observer in the laboratory frame, a high-speed region will alternate with a low-speed region. Since a burst will occur only at the end of a low-speed region, the experimental burst detection techniques will indicate $2\lambda_x$ for the wavelength in the wall region and λ_x in the outer region. The observed phase shift in the z direction will also imply a reversal of the direction of rotation of the longitudinal vortices near a line of instabilities (see figures 1 and 4). The reason for this is not clear at the moment.

We now turn to the last element in the model. It provides an explicit coupling mechanism between the wall region and the outer region by way of ejected fluid brought into the outer region by the burst events in the wall region. The burst events are assumed to run in phase with the outer structures (Brown & Thomas 1977). Hence the trajectory of the ejected fluid will have an almost fixed position with respect to the large-scale structures in which new vorticity is created. A second coupling mechanism, which is equally important in our opinion, arises out of the influence the outer layer

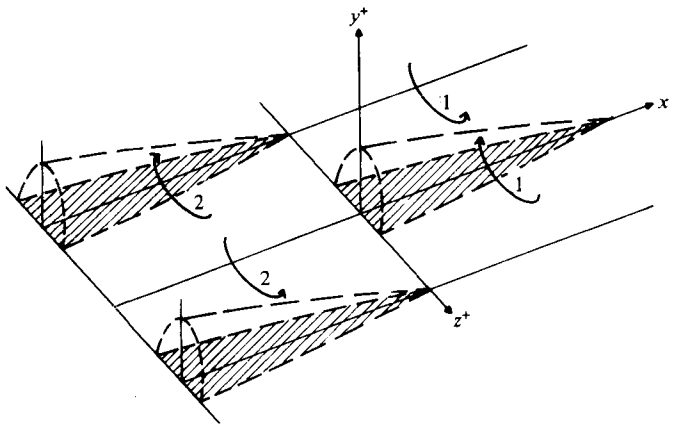

FIGURE 4. The relative position of low-speed streaks (the edge is marked by a dashed line) in two successive cycles. The arrows 1 and 2 indicate the direction of rotation of the longitudinal vortices.

has on the wall layer. This can take two forms: one has to do with the periodicity of the pressure created by the outer structures and the other is a consequence of the so-called sweep event which brings in high-momentum fluid from the edge of the wall layer. These are difficult questions to handle in the framework of the present discussion and we will relegate them to subsequent sections for more detailed consideration.

Figure 5 is a schematic representation of the proposed model for the complete boundary layer. It clearly indicates the assumed phase relation between inner and outer regions.

3. Analysis of the model

In this section, the time-dependent Navier–Stokes equations will be used to derive equations corresponding to the physical model described above. Attention is limited to a zero pressure gradient flow over a smooth flat plate. Since the primary interest here is on time evolution of large-scale structures, the flow field is split, instead of the usual Reynolds decomposition, into a large-scale and a small-scale part, both of which will be functions of time. The large-scale quantities scale on the distance between successive burst events λ_x, while the small-scale fluctuations have a length scale λ' and these are assumed to be important only in burst events. The different scales relevant to the problem are illustrated in figure 6.

The following averaging procedure is adopted to obtain the equations governing the large-scale flow field:

$$\tilde{\mathbf{u}}(\mathbf{r},t) = \frac{1}{l_i}\int_{x-\frac{1}{2}l_i}^{x+\frac{1}{2}l_i} \mathbf{u}\,dx, \quad \tilde{p}(\mathbf{r},t) = \frac{1}{l_i}\int_{x-\frac{1}{2}l_i}^{x+\frac{1}{2}l_i} p\,dx. \tag{3}$$

The small-scale quantities are defined as

$$\mathbf{u}''(\mathbf{r},t) = \mathbf{u} - \tilde{\mathbf{u}} \quad \text{and} \quad p''(\mathbf{r},t) = p - \tilde{p}. \tag{4}$$

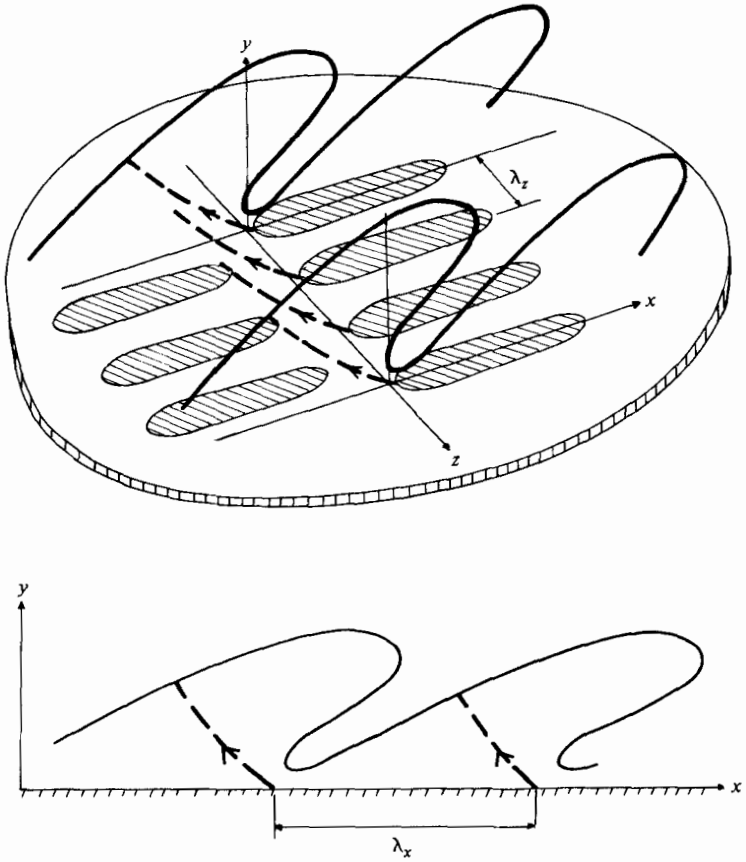

FIGURE 5. A composite picture of the proposed structures in a turbulent boundary layer. The dashed lines are the trajectories of the ejected fluid parcels. The shaded areas represent the low-speed streaks.

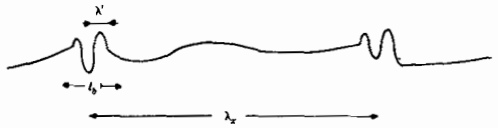

FIGURE 6. The different scales in a typical cycle. λ_x is the mean distance between two bursts, l_b is the width of a burst region and λ' is the length scale of the fluctuations in a burst.

This averaging procedure has the advantage that the different flow quantities retain their meaning in the moving frame which is employed in the rest of the work. The integration length l_i defines the resolution that can be obtained in the large-scale quantities. The decomposition procedure used is equivalent to low-pass filtering of turbulence signals, a technique that is commonly employed in experiments to isolate large-scale and small-scale fluctuations (cf. Blackwelder & Kaplan 1972).

The averaged equations of motion are

$$\frac{\partial \tilde{\mathbf{u}}}{\partial t} + \tilde{\mathbf{u}} \cdot \nabla \tilde{\mathbf{u}} = -\frac{1}{\rho} \nabla \tilde{p} + \nu \nabla^2 \tilde{\mathbf{u}} - \nabla \cdot \widetilde{(\mathbf{u}'' \mathbf{u}'')}, \tag{5}$$

$$\nabla.\tilde{\mathbf{u}} = 0. \tag{6}$$

The following approximations have been used while deriving equations (5) and (6):

$$\frac{1}{l_i}\int_{x-\frac{1}{2}l_i}^{x+\frac{1}{2}l_i} \tilde{\mathbf{u}}\tilde{\mathbf{u}}\,dx = \tilde{\mathbf{u}}\tilde{\mathbf{u}}, \quad \frac{1}{l_i}\int_{x-\frac{1}{2}l_i}^{x+\frac{1}{2}l_i} \mathbf{u}''\tilde{\mathbf{u}}\,dx = \frac{\tilde{\mathbf{u}}}{l_i}\int_{x-\frac{1}{2}l_i}^{x+\frac{1}{2}l_i} \mathbf{u}''\,dx = 0. \tag{7}$$

The procedure is valid for $\lambda_x \gg l_i \gg \lambda'$. This condition is realizable in turbulent boundary layers, since λ_x/l_b is about 20 (Blackwelder & Kaplan 1972) and each burst event consists of only a few small-scale wavelengths λ'. Thus λ_x/λ' is of the order 100.

Equations (5) and (6) for the large-scale motion are the counterpart of the Reynolds equations for the mean motion and contain small-scale stress terms as unknowns. It is assumed that these terms are important only in the burst regions which occupy a small fraction of the total flow field.

Since the burst regions travel downstream with a constant velocity U_c, an *almost* stationary picture emerges in a moving co-ordinate frame. Applying the transformations

$$\left.\begin{aligned} &\tilde{\mathbf{u}}_c = (U_c - \tilde{u}, \tilde{v}_c(=\tilde{v}), \tilde{w}_c(=\tilde{w})), \quad \tilde{p}_c = \tilde{p} \\ \text{and} \quad &\mathbf{r}_c = (U_c t - x, y_c(=y), z_c(=z)), \end{aligned}\right\} \tag{8}$$

we obtain

$$\frac{\partial\tilde{\mathbf{u}}_c}{\partial t_c} + \tilde{\mathbf{u}}_c.\nabla\tilde{\mathbf{u}}_c = -\frac{1}{\rho}\nabla\tilde{p}_c + \nu\nabla^2\tilde{\mathbf{u}}_c - [\nabla.\widetilde{(\mathbf{u}''\mathbf{u})''}].\mathbf{I}^*, \tag{9}$$

$$\nabla.\tilde{\mathbf{u}}_c = 0, \tag{10}$$

where

$$\mathbf{I}^* = \begin{pmatrix} -1 & 0 & 0 \\ 0 & 1 & 0 \\ 0 & 0 & 1 \end{pmatrix}.$$

The transformed boundary conditions are

$$\left.\begin{aligned} &\tilde{\mathbf{u}}_c = (U_c - u_\infty, 0, 0) \quad \text{for} \quad \mathbf{r}_c = (x_c, \infty, z_c), \\ &\tilde{\mathbf{u}}_c = (U_c, 0, 0) \quad \text{for} \quad \mathbf{r}_c = (x_c, 0, z_c). \end{aligned}\right\} \tag{11}$$

Since the small-scale stress $\widetilde{\mathbf{u}''\mathbf{u}''}$ is localized in a narrow region, the integrated effect of the x derivatives of this term is zero. Thus the x derivatives of $\widetilde{\mathbf{u}''\mathbf{u}''}$ will have no influence on the large-scale motion and are neglected in what follows.

3.1. *Order-of-magnitude estimates*

The order-of-magnitude analysis is carried out on the two-dimensional version of the governing equations (9) and (10). As in the case of the postulated physical model, such a procedure would only be valid for the description of the outer structures. Three-dimensional effects are expected to play a significant role in the wall-region processes. Because of inadequate information on these effects, it is not possible to prescribe appropriate boundary conditions for the spanwise flow variables. This makes it difficult to incorporate these effects in the framework of the formalism we use in the order-of-magnitude analysis. However, these effects will be included in a

parametric form in the calculations to be presented later. Since the secondary motion of the longitudinal vortices is very weak, they will not affect the essentials of the arguments developed here. This is more or less in conformity with the practice followed in handling boundary-layer flows in corners (Mager 1964).

Two factors about the present flow problem need to be specially stressed before presenting the analysis. The first one arises out of periodicity of the structures, and our main concern in this work is about the time evolution of these structures over a couple of periods at most. The maximum x-scale we are interested in, therefore, is $2\lambda_x$. Since this period scales on the boundary-layer thickness, boundary-layer growth will be insignificant and the mean flow will exhibit features of essentially parallel flow. The second factor is to do with the small-scale turbulent stress term in equation (9). Its presence is felt over only highly localized regions and it thus provides a compact source term in the equation. These two factors have an important bearing on the choice of scales for the relevant variables.

The first step in the analysis is to define a set of dimensionless variables. For the space variables, we define

$$x_c^* = \frac{x_c}{\beta_1 \lambda_x}, \quad y_c^* = \frac{y_c}{\beta_2 \lambda_x}, \tag{12}$$

where β_1 and β_2 are dimensionless scaling factors to be determined as part of the analysis.

In order to obtain appropriate magnitude estimations for $\tilde{u}_c$ we note that it is made up of a mean part which exhibits a parallel flow character and a fluctuating large-scale part,

$$\tilde{u}_c = \bar{u}_c + \tilde{u}_c'; \tag{13}$$

$\bar{u}_c$ is of the order of magnitude of u_∞. This follows from $\bar{u}_c = U_c - \bar{u}$, where the convection velocity U_c has a value of about $0{\cdot}8u_\infty$; $\tilde{u}_c'$ is of the order of magnitude of u_*. Therefore for an individual structure $\partial\tilde{u}_c/\partial x_c$ is dominated by $\partial\tilde{u}_c'/\partial x_c$ and $\partial\tilde{u}_c/\partial y_c$ by $\partial\bar{u}_c/\partial y_c$. Thus we use the following expressions for the derivatives concerned:

$$\frac{\partial\tilde{u}_c}{\partial x_c} = \frac{u_*}{\beta_1\lambda_x}\frac{\partial\tilde{u}_c^*}{\partial x_c^*} \quad \text{and} \quad \frac{\partial\tilde{u}_c}{\partial y_c} = \frac{u_\infty}{\beta_2\lambda_x}\frac{\partial\tilde{u}_c^*}{\partial y_c^*}. \tag{14}$$

From the continuity equation we obtain the following scaling for $\tilde{v}_c$:

$$\tilde{v}_c^* = \tilde{v}_c \Big/ \left(\frac{\beta_2}{\beta_1} u_*\right). \tag{15}$$

The second factor we mentioned earlier leads to the non-dimensionalization of small-scale turbulent stress terms in the following manner:

$$(\widetilde{u''v''})^* = \frac{\widetilde{u''v''}}{(\lambda_x/l_b)\,u_*^2}, \quad (\widetilde{v''^2})^* = \frac{\widetilde{(v''^2)}}{(\lambda_x/l_b)\,u_*^2}. \tag{16}$$

The last variable that needs to be non-dimensionalized is the time variable. Noting that the time variable enters into our model only through the presence of turbulent fluctuations, we define

$$t_c^* = \frac{t_c}{\beta_1\lambda_x/u_*}. \tag{17}$$

Equation	Equality	Physical interpretation	Label in figure 7
x momentum	$\beta_1 = 1/R_\lambda$	x viscous stress = convection	2
	$\beta_1 = R_\lambda \beta_2^2 \frac{u_*}{u_\infty}$	y viscous stress = convection	3
	$\beta_1 = \beta_2 \frac{u_\infty}{u_*} \frac{l_b}{\lambda_x}$	small-scale turbulent stress = convection	1
	$\beta_2 = \frac{1}{R_\lambda} \frac{u_\infty^2}{u_*^2} \frac{l_b}{\lambda_x}$	small-scale turbulent stress = y viscous stress	(8)
y momentum	$\beta_1 = \beta_2$	pressure gradient = x convection	4
	$\beta_1 = 1/R_\lambda$	x viscous stress = x convection	6
	$\beta_1 = R_\lambda \beta_2^2$	y viscous stress = x convection	7
	$\beta_1 = \beta_2 \left(\frac{u_\infty}{u_*} \frac{l_b}{\lambda_x}\right)^{\frac{1}{2}}$	small-scale turbulent stress = x convection	5
	$\beta_1 = \frac{1}{R_\lambda} \frac{u_\infty}{u_*^2} \frac{l_b}{\lambda_x}$	small-scale turbulent stress = y viscous stress	(9)

Note: The order symbols have been suppressed for convenience.

TABLE 1. Order equalities.

Introducing definitions (12), (14), (15), (16) and (17) into the two-dimensional version of equations (9), the following non-dimensional† momentum equations are obtained:

$$\frac{\partial \tilde{u}_c^*}{\partial t_c^*} + \tilde{u}_c^* \frac{\partial \tilde{u}_c^*}{\partial x_c^*} + \tilde{v}_c^* \frac{\partial \tilde{u}_c^*}{\partial y_c^*} = -\frac{p_r}{\rho u_* u_\infty} \frac{\partial \tilde{p}_c^*}{\partial x_c^*} + \frac{1}{R_\lambda \beta_1} \frac{\partial^2 \tilde{u}_c^*}{\partial x_c^{*2}} + \frac{\beta_1}{R_\lambda \beta_2^2} \frac{u_\infty}{u_*} \frac{\partial^2 \tilde{u}_c^*}{\partial y_c^{*2}} + \frac{\lambda_x}{l_b} \frac{u_*}{u_\infty} \frac{\beta_1}{\beta_2} \frac{\partial (\widetilde{u''v''})^*}{\partial y_c^*},$$

$$\frac{u_*}{u_\infty} \frac{\partial \tilde{v}_c^*}{\partial t_c^*} + u_c^* \frac{\partial \tilde{v}_c^*}{\partial x_c^*} + \frac{u_*}{u_\infty} \tilde{v}_c^* \frac{\partial \tilde{v}_c^*}{\partial y_c^*} = -\frac{p_r}{\rho u_* u_\infty} \frac{\beta_1^2}{\beta_2^2} \frac{\partial \tilde{p}_c^*}{\partial y_c^*} + \frac{1}{R_\lambda \beta_1} \frac{\partial^2 \tilde{v}_c^*}{\partial x_c^{*2}} + \frac{\beta_1}{R_\lambda \beta_2^2} \frac{\partial^2 \tilde{v}_c^*}{\partial y_c^{*2}} + \frac{\lambda_x}{l_b} \frac{u_*}{u_\infty} \frac{\beta_1^2}{\beta_2^2} \frac{\partial (\widetilde{v''^2})^*}{\partial y_c^*}, \quad (18)$$

where $R_\lambda = \lambda_x u_\infty / \nu$ is the Reynolds number and p_r is the characteristic magnitude of pressure fluctuations.

Since the pressure term is expected to balance the convective terms in the x-momentum equation, we assume $p_r/\rho u_* u_\infty$ to be of order unity. This appears to conflict with the more usual scaling of pressure fluctuations on ρu_*^2. This scaling property is not, however, well established. Willmarth (1975*b*) summarizes available data and shows an increase of $p'/\rho u_*^2$ with Reynolds number. Townsend (1976) arrives at a similar conclusion on the basis of theoretical arguments. Dinckelakker *et al.* (1977) measured pressure waves with an amplitude up to $0{\cdot}5 \rho u_* u_\infty$ (which corresponds to

† The normalization has been carried out with respect to the x-convection term in each equation.

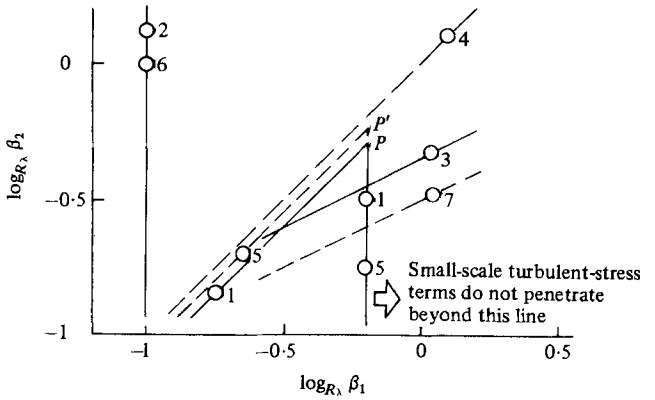

FIGURE 7. Order relations for the $\tilde{u}_c$ (solid lines) and $\tilde{v}_c$ (dashed lines) equations. The numbers in circles correspond to those in table 1. $R_\lambda = 10^5$, $u_\infty/u_* = 30$ and $\lambda_x/l_1 = 10$.

$12\rho u_*^2$ for their flow conditions). This indicates that the estimate $p_r/\rho u_*^2 u_\infty = O(1)$ is more accurate than $p_r/\rho u_*^2 = O(1)$.

Equations (18) can be used to generate a set of ordering relations, the more important of which are tabulated in table 1. These relations plot as straight lines on a $\log_{R_\lambda} \beta_1$, $\log_{R_\lambda} \beta_2$ plot (figure 7). The diagram has been constructed for $u_\infty/u_* = 30$, $\lambda_x/l_b = 10$ and $R_\lambda = 10^5$. Along each line two terms in an equation have the same order of magnitude. Far from a line one of the two terms under consideration is much smaller than the other. The plot can be used to identify different regions of flow where certain terms can be ignored, to the leading order of approximation.

The x-scales that are smaller than l_b correspond to fluctuations in the burst regions that have been eliminated by the averaging procedure. The smallest x-scale for which the equations make sense is l_b. This implies that all scales of interest are to the right of lines 2 and 6 in figure 7, which means that viscous x diffusion can be neglected in both equations.

Two situations can be distinguished for the x-scale: $\beta_1 = l_b/\lambda_x$ and $\beta_1 > l_b/\lambda_x$. In the latter case, small-scale turbulent stress can be neglected (to the right of lines 1 and 5). On lines 1 and 5 ($\beta_1 = l_b/\lambda_x$), the small-scale stresses and the convective terms are of equal importance.

The region for which $\beta_1 > l_b/\lambda_x$ contains the lines 3, 4 and 7. On line 4 the pressure gradient term in the $\tilde{v}_c$ equation is in balance with the convective term and since we are above lines 3 and 7 the viscous y diffusion can be neglected in the x- and y-momentum equations, respectively. In other words: the inviscid approximation holds along line 4.

Closer to the wall, along line 3, the viscous y diffusion has to be included in the $\tilde{u}_c$ equation, but now we are below line 4 which means that the pressure gradient is the only remaining term in the equation for $\tilde{v}_c$ (the viscous term is always small compared with the pressure gradient in this region). Here the well-known 'boundary-layer approximation' holds. Line 7 is of less importance because it relates viscous and convective effects that are both small compared with the pressure gradient in this region.

For $\beta_1 = l_b/\lambda_x$ the situation is equivalent, except that along lines 1 and 5 the small-

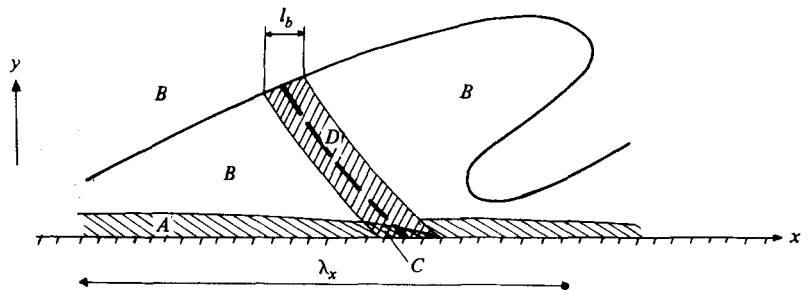

FIGURE 8. The location of the different regions in the boundary layer. A and C form the wall layer, B and D the outer region. The small-scale turbulent stress is important in the regions C and D only.

scale stress terms have to be included in the equations. The small-scale stress is not important throughout the boundary layer; in the $\tilde{u}_c$ equation its importance is limited to $\beta_2 \leqslant u_*/u_\infty$ (point P in figure 7) and in the $\tilde{v}_c$ equation to $\beta_2 \leqslant (l_b u_*/\lambda_x u_\infty)^{\frac{1}{2}}$ (point P'). To find this the value $\beta_1 = l_b/\lambda_x$ has been substituted in the order relations 1 and 5.

The foregoing considerations lead to the definition of four regions, indicated by A, B, C and D in figure 8. The leading-order equations for the regions C and D in the limit of large R_λ are as follows.

$$\left.\begin{aligned} &\textit{Region } C\text{:}\quad \beta_1 = l_b/\lambda_x,\quad \beta_2 \leqslant \left(\frac{1}{R_\lambda}\frac{u_\infty}{u_*}\beta_1\right)^{\frac{1}{2}},\\ &\frac{\partial \tilde{u}_c}{\partial t_c} + \tilde{u}_c\frac{\partial \tilde{u}_c}{\partial x_c} + \tilde{v}_c\frac{\partial \tilde{u}_c}{\partial y_c} = -\frac{1}{\rho}\frac{\partial \tilde{p}_c}{\partial x_c} + \frac{\partial(\widetilde{u''v''})}{\partial y_c} - \frac{\partial^2 \tilde{u}_c}{\partial y_c^2},\\ &\frac{1}{\rho}\frac{\partial \tilde{p}_c}{\partial y_c} = \frac{\partial(\widetilde{-v''^2})}{\partial y_c},\quad \frac{\partial \tilde{u}_c}{\partial x_c} + \frac{\partial \tilde{v}_c}{\partial y_c} = 0. \end{aligned}\right\} \tag{19}$$

$$\left.\begin{aligned} &\textit{Region } D\text{:}\quad \beta_1 = l_b/\lambda_x,\quad \beta_2 > \left(\frac{1}{R_\lambda}\frac{u_\infty}{u_*}\beta_1\right)^{\frac{1}{2}},\\ &\frac{\partial \tilde{u}_c}{\partial t_c} + \tilde{u}_c\frac{\partial \tilde{u}_c}{\partial x_c} + \tilde{v}_c\frac{\partial \tilde{u}_c}{\partial y_c} = -\frac{1}{\rho}\frac{\partial \tilde{p}_c}{\partial x_c} + \frac{\partial(\widetilde{u''v''})}{\partial y_c},\\ &\left(\frac{\partial \tilde{v}_c}{\partial t_c}\right)^{\dagger} + \tilde{u}_c\frac{\partial \tilde{v}_c}{\partial x_c} + \tilde{v}_c\frac{\partial \tilde{v}_c^{\dagger}}{\partial y_c} = -\frac{1}{\rho}\frac{\partial \tilde{p}_c}{\partial y_c} + \frac{\partial(\widetilde{-v''^2})}{\partial y_c},\\ &\frac{\partial \tilde{u}_c}{\partial x_c} + \frac{\partial \tilde{v}_c}{\partial y_c} = 0. \end{aligned}\right\} \tag{20}$$

The equations for regions A and B ($\beta_1 > l_b/\lambda_x$) are the same as (19) and (20) respectively, but with the small-scale turbulent stress terms omitted. Note that the x-derivatives have been neglected according to the arguments given below equation (11).

The physical meaning of the different regions becomes clear from an examination of figure 8. In region A the wall transfers momentum deficit to a thin layer by means of viscous forces. This layer is ejected in region C, where the small-scale turbulent

† (u_∞/u_*) factors multiply these terms in equation (18), but the terms have been included nonetheless for ease of application of the solution method.

stress as well as viscous forces are important, and the momentum deficit is transferred to the outer layer in region D. Region B is free of both viscous and small-scale turbulent stresses.

A more significant outcome of the analysis presented is that it provides estimates of distances (in the normal direction) to which different physical effects penetrate. The momentum transfer takes place by three effects.

(*a*) Viscous forces in the wall layer penetrate to

$$y_c = \left(\frac{1}{R_\mu}\frac{u_\infty}{u^*}\right)^{\frac{1}{2}} \lambda_x.$$

(*b*) Wall-layer ejections contribute small-scale stresses to a distance

$$y_c = \lambda_x \frac{u_*}{u_\infty}$$

(point P in figure 7).

(*c*) The thickness of the boundary layer is of the order of λ_x (actually $\frac{1}{2}\lambda_x$ as known from experiments).

For $u_*/u_\infty = 1/30$ and $R_\lambda = 10^5$, these effects penetrate to 58, 111 and 1670, respectively, in y^+ units.

4. Solution procedure

While considerable simplification has been achieved in the preceding section, it is still necessary to introduce closure assumptions for constructing a complete solution to the problem. The closure problem is particularly severe in regions C and D where the small-scale turbulent stress terms play a vital part. Since the intention of the present work is to seek clarifications about the dynamics of coherent structures rather than provide a scheme of predictive capability, we shall not be concerned with detailed questions about closure hypotheses. Instead, we shall concentrate on regions A and B which can be solved with inputs from well-documented experimental data. A simple model will be used to determine the influence of burst events in region D on the behaviour of structures in the outer region B.

The wall-layer equations can be solved for region A by specifying the velocity profile just after the occurrence of a burst. This profile can be derived from available experimental data and is used as an initial condition for the boundary-layer equations. In the moving frame, the pressure gradient imposed by the outer region on the wall layer can be expected to be independent of time. Thus the wall layer problem is stationary and the relevant equations are

$$\left.\begin{aligned} \tilde{u}_c\frac{\partial \tilde{u}_c}{\partial x_c} + \tilde{v}_c\frac{\partial \tilde{u}_c}{\partial y_c} &= u_{cr}\frac{\partial u_{cr}}{\partial x_c} + \nu\frac{\partial^2 \tilde{u}_c}{\partial y_c^2}, \\ \frac{\partial \tilde{u}_c}{\partial x_c} + \frac{\partial \tilde{v}_c}{\partial y_c} &= 0. \end{aligned}\right\} \tag{21}$$

The boundary conditions are

$$\left.\begin{aligned} &\tilde{u}_c = U_c, \quad \tilde{v}_c = 0 \quad \text{for} \quad y_c = 0, \\ &\tilde{u}_c = u_{cr}(x_c) \quad\quad\;\; \text{for} \quad y_c \to \infty, \\ &\tilde{u}_c = U_c - u_0(y_c) \quad \text{for} \quad x_c = 0. \end{aligned}\right\} \tag{22}$$

The pressure gradient term $u_{cr}\,\partial u_{cr}/\partial x_c$ has to be found by matching the inner and outer solutions. Some comments will be made later on the difficulties in adopting such a procedure; the solutions presented in this paper have been obtained by treating this term as known. The equations (21) and (22) have been transformed using Falkner–Skan variables and the resulting equations have been solved by the 'Keller Box method' (Cebeci & Smith 1974).

The outer layer equations corresponding to region B and D are elliptic and therefore more difficult to handle. Region B, in which no closure assumption is needed, cannot be solved independently of D. The bursts from the wall region bring in additional vorticity which plays a vital role in controlling the dynamics of the outer structures. According to the model this vorticity is generated in region D only. A convenient method of handling this problem is by the 'discrete vortex structures' which have been successfully used in the study of large-scale structures in free shear layers (Acton 1976; Clements 1977). The application of the method to the present problem will be discussed first before going into the question of the calculation of added vorticity.

The equations are written in terms of vorticity and stream function:

$$\left.\begin{aligned} \frac{\partial\tilde{\omega}_c}{\partial t_c}+\tilde{u}_c\frac{\partial\tilde{\omega}_c}{\partial x_c}+\tilde{v}_c\frac{\partial\tilde{\omega}_c}{\partial y_c} &= \frac{\partial(\widetilde{-v''^2})}{\partial y_c\,\partial x_c}-\frac{\partial^2(\widetilde{u''v''})}{\partial y_c^2}, \\ \frac{\partial^2\tilde{\psi}_c}{\partial x_c^2}+\frac{\partial^2\tilde{\psi}_c}{\partial y_c^2} &= -\tilde{\omega}_c. \end{aligned}\right\} \tag{23}$$

The source term on the right-hand side of the vorticity equation represents the vorticity added per time unit by the ejection jets. The continuous vorticity distribution in the (x_c, y_c) plane is approximated by a number of line vortices (with their axes along the spanwise direction). Thus

$$\omega_c = \sum_{n=1}^{N}(-\kappa_n)\,\delta(x_c-x_n)\delta(y_c-y_n), \tag{24}$$

where κ_n is the strength and (x_n, y_n) the position of the nth line vortex. The solution for $\tilde{\psi}_c$ is given by the Green's function for the Poisson equation,

$$\tilde{\psi}_c(x,y) = \sum_{n=1}^{N}\frac{\kappa_n}{4\pi}\ln\{(x_c-x_n)^2+(y_c-y_n)^2\}. \tag{25}$$

With a given distribution of line vortices, the velocity at each vortex centre is calculated from (25) as the velocity induced by all other vortices. The position of the vortex centre one time step later is calculated by assuming that the vortices are convected along streamlines (which is, incidentally, what the left-hand side of the first of equations (23) says). A second-order extrapolation formula is used for this purpose and this is given as

$$\left.\begin{aligned} x_n(t+dt) &= x_n(t)+\tfrac{1}{2}[3u_n(t)-u_n(t-dt)], \\ y_n(t+dt) &= y_n(t)+\tfrac{1}{2}[3v_n(t)-v_n(t-dt)]. \end{aligned}\right\} \tag{26}$$

To limit the number of operations at each time step, only one or two periods of the boundary layer are considered. Although the periods immediately preceding and following the one that is calculated are in an earlier and later stage of development, respectively, it is assumed that the differences between them are small. This is really

a consequence of the parallel flow approximation mentioned earlier. If the x interval under consideration is extended periodically with wavelength a (a can be λ_x or $2\lambda_x$), part of the summation in (25) can be performed analytically. The velocity induced at (x_c, y_c) by an infinite row of vortices with strength κ and spacing a at positions (x_0, y_0), $(x_0 \pm a, y_0)$, $(x_0 \pm 2a, y_0)$, etc., is (Lamb 1932)

$$\tilde{u}_c(x_c, y_c) = \frac{\kappa \sinh 2\pi(y_c - y_0)\, a^{-1}}{2a[\cosh 2\pi(y_c - y_0)\, a^{-1} - \cos 2\pi(x_c - x_0)\, a^{-1}]},$$

$$\tilde{v}_c(x_c, y_c) = \frac{-\kappa \sin 2\pi(x_c - x_0)\, a^{-1}}{2a[\cosh 2\pi(y_c - y_0)\, a^{-1} - \cos 2\pi(x_c - x_0)\, a^{-1}]}. \tag{27}$$

The actual velocity at any point is determined by adding the contribution of all the vortices in the interval a.

When two vortices are very close to each other, the singularity at the vortex centre produces very large velocities there. This is held to be responsible for the rather chaotic motion predicted by the method for the mixing-layer problem. This has been overcome by using a finite core radius for the vortex elements as suggested by Chorin & Bernard (1972); the relevant stream functions in this formulation are

$$\left.\begin{aligned} \tilde{\psi}_c &= \frac{\kappa}{2\pi} \ln r \quad \text{for} \quad r > \sigma, \\ \tilde{\psi}_c &= \kappa \left(\frac{r}{2\pi\sigma} + C_2 \right) \quad \text{for} \quad r \leqslant \sigma, \end{aligned}\right\} \tag{28}$$

where $C_2 = (2\pi)^{-1}(\ln \sigma - 1)$ for continuity of $\tilde{\psi}_c$ at $r = \sigma$, r is the distance from the vortex centre and σ the core radius.

The boundary condition $\tilde{v}_c = 0$ at $y_c = 0$ is satisfied by adding mirror-image elements to all the vortices. The no-slip condition at the wall is, of course, accounted for by the wall layer. The optimum values for σ and Δt as determined by Acton (1976) have been used and their dimensionless values are $\sigma/\lambda_x = 0{\cdot}07$ and $dt/(\lambda_x \Delta u) = 0{\cdot}05$, where

$$\Delta u = a^{-1} \sum_{n=1}^{N} \kappa_n,$$

and N is the number of vortices in the interval a.

As per the model postulated in §2, the inner and outer solutions do not exist independently, but interact with each other. Two types of interactions are visualized – one passive and the other active. Both these types of interaction pose considerable problems and at the present moment do not lend themselves to rigorous mathematical treatment. We now treat these questions in some detail.

The passive interaction mentioned above is concerned with the matching of the inner and outer solutions. The usual procedure for this matching, i.e. equating the inner limit of the outer solution and the outer limit of the inner solution, cannot be adopted since the velocity profile in the overlap region is expected to possess a logarithmic behaviour (see, for example, Fendell 1972; Mellor 1972; Tennekes 1968). The appropriate procedure in such a situation is of course to match the two solutions on an intermediate scale (Van Dyke 1975). Even for this procedure we require the limiting behaviour of the two solutions. The numerical solutions computed here

unfortunately do not permit an investigation of this limiting behaviour. The discrete vortex approximation does not provide accurate solutions close to the wall because of inadequate resolution. The wall layer solution, on the other hand, is completely determined for large y-values by the imposed initial condition. Thus the velocity at the edge of the wall layer is treated as a known quantity to be determined by experiment.

The active interaction between the two layers is related to the burst events which bring the low-momentum fluid from the wall region to the outer layer. According to the model presented in this work, these 'ejection jets' are vital for the determination of the dynamics of the outer structures. However, very little is known about the interactions between the ejected fluid and the outer layer. As such we are forced to make some *ad hoc* assumptions about this interaction.

In the moving frame, it is convenient to use a Lagrangian description for calculating the trajectory of the fluid parcel released by the instability zones. The trajectory itself is determined by the initial velocity and a damping mechanism assumed to be proportional to the difference in velocities of the ejected fluid and the surrounding fluid. Although this model cannot be realistic in all details it has an important observed characteristic, namely that it simulates the large-amplitude pulses in the Reynolds shear stress (the source term in (23)). In this way we can investigate the influence of the burst events on the large-scale structures in outer region. The governing equations for the motion are

$$\left.\begin{aligned} \frac{d^2X_{bc}}{dt^2}(t,t_0) &= -c_x\left[\frac{dX_{bc}}{dt}(t,t_0)-\tilde{u}_c(X_{bc},Y_{bc},t)\right],\\ \frac{d^2Y_{bc}}{dt^2}(t,t_0) &= -c_y\left[\frac{dY_{bc}}{dt}(t,t_0)-\tilde{v}_c(X_{bc},Y_{bc},t)\right]. \end{aligned}\right\} \tag{29}$$

In these equations X_{bc}, $Y_{bc}(t,t_0)$ denote the co-ordinates at time t of the fluid parcel that left the wall region at time t_0. The initial conditions in the moving frame are

$$\left.\begin{aligned} X_{bc}(t_0,t_0) &= X_{bc0}, \quad (dX_{bc}/dt)_{t_0,t_0} = u_{bc0},\\ Y_{bc}(t_0,t_0) &= 0, \qquad (dY_{bc}/dt)_{t_0,t_0} = v_{bc0}. \end{aligned}\right\} \tag{30}$$

Since $\tilde{u}_c$ and $\tilde{v}_c$ are generated numerically, equations (29) and (30) require numerical solution. At each time step the position and velocity of a new lump of fluid are stored in the memory of the computer. One time step later the velocities and positions of all the fluid parcels† in the 'ejection jet' are expressed in terms of those of the previous time, making use of the solution of (23), which is valid between two time levels, with the assumption that $\tilde{u}_c$ and $\tilde{v}_c$ do not change over one time step. The trajectory computation is terminated when the velocity difference between the fluid in the ejection jet and the surrounding fluid attains a prescribed small value. The memory location thus released is used for a newly ejected fluid parcel.

The vorticity added to the large-scale field during one time step is given by

$$d\omega_c = \left[\frac{\partial^2(\widetilde{-v''^2})}{\partial y_c\,\partial x_c} - \frac{\partial^2(\widetilde{u''v''})}{\partial y_c^2}\right]dt, \tag{31}$$

where $u'' = -(u_{bc}-\tilde{u}_c)$, $v_c'' = (v_{bc}-\tilde{v}_c)$.

† Note that in the moving frame the ejection is assumed to occur continuously.

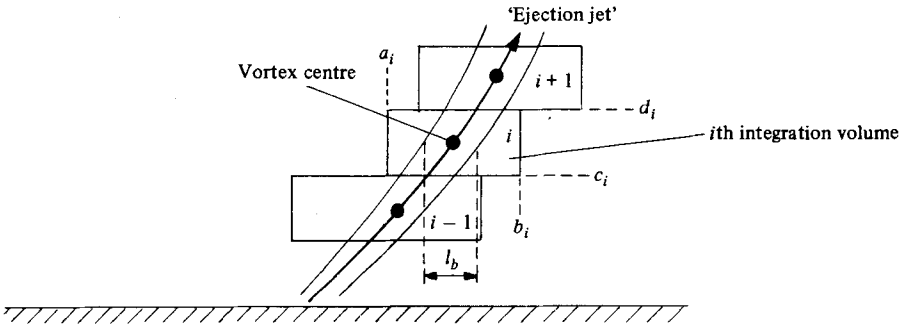

FIGURE 9. The integration volumes around the 'ejection jets'.

The discrete representation of this added vorticity is obtained by integrating (31) over a volume around the jet as shown in figure 9. The first term in (31) does not contribute anything to the integral if it is assumed that u'' and v'' are independent of x_c inside the jet and zero everywhere else. The final result then is

$$\Delta\omega_i = -\Delta t \left.\frac{\partial l_b \widetilde{(u''v'')}}{\partial y_c}\right|_{c_i}^{d_i}. \tag{32}$$

The quantity l_b denotes the width of the jet in a cross-section parallel to the wall. The product $l_b v_{bc}$ is constant because of continuity requirements; in other words l_b varies with y_c.

The source term in equation (23) is handled by adding new vortex elements at each time step, representing the vorticity generated by the ejection jets in the outer layer. In order to limit the number of discrete vortices thus added, the number of integration volumes is held to four. This number is small compared with the total number of vortices, which is equal to 48 for $a = \lambda_x$. The total number of vortices is kept constant by joining vortex elements that are very close to each other. The problem of choosing appropriate values for the different parameters will be dealt with in the next section.

5. Results

The main purpose of the calculations carried out here is to elucidate the dynamics of coherent structures in a wall-bounded turbulent flow. To this end we address ourselves to three specific questions. The first one is concerned with the mechanism responsible for periodic regeneration of the bursts. It is hypothesized in this connection that the conditions for the formation of a burst are realized if an inflectional velocity profile is formed in the wall layer towards the end of a period. The second question has to do with the mechanisms that are required to maintain the structures in the outer layer. The last and probably the most important question is whether these structures can explain the transport processes – in particular, the momentum transport – in a turbulent boundary layer.

During the course of the work a substantial amount of computational results have been accumulated. A few of these are available elsewhere (Van Dongen, Beljaars & De Vries 1978; Beljaars 1978, 1979). Here we shall satisfy ourselves with results that directly shed light on the questions raised above.

5.1. *Wall-layer results*

To derive quantitative results from the model, several 'input parameters' need to be specified. For the wall layer these are: the convection velocity U_c, the mean burst interval $\bar{T}_b$ and the initial profile $u_0(y_c)$. This information has been derived from experiments in boundary layers on smooth walls for zero or small pressure gradients. Some of these results have been presented in terms of wall variables and others in terms of outer variables. To facilitate calculations presented here, the experimental results have been converted from one to the other variable (as and where necessary) using the following empirical friction law (Hinze 1975)

$$\frac{c_f}{2} = \left(\frac{u_*}{u_\infty}\right)^2 = 0{\cdot}012R^{-0{\cdot}25} \quad \text{with} \quad \delta = 10{\cdot}9\delta_m, \tag{33}$$

where $R = u_\infty \delta_m/\nu$, δ is the thickness of the boundary layer and δ_m the momentum loss thickness. R is used as an independent parameter and a range of values around 3000 has been considered.

The convection velocity U_c has been measured by many methods. Favre, Gaviglio & Dumas (1967) derived U_c for large eddies from space–time correlation measurements. Willmarth & Woolridge (1962) and Wills (1971) measured the convection velocity of the burst events directly. These measurements suggest $U_c \simeq 0{\cdot}8u_\infty$ and this value has been chosen for the present calculations.

The review of Laufer & Badri Narayanan (1971) and the more recent work of Ueda & Hinze (1975) suggest that the mean burst interval is given by $\bar{T}_b u_\infty/\delta = 5$ in the wall region and 2·5 in the outer region. As pointed out earlier, the outer period is believed to be the appropriate value to be used in the present calculations. However, for purposes of checking this hypothesis both values have been used.

The initial velocity profile $u_0(y)$ has been assumed for preliminary calculations to coincide with the assumption of Einstein & Li (1956). The assumption is that the momentum exchange in a burst event is so effective that a uniform velocity profile is established right up to the wall. The value of the velocity is itself derived from the assumption that the fluid which replaces the ejected fluid originates in the buffer region and is given by

$$u_0^+(y) = 2{\cdot}5 \ln y_r^+ + 5{\cdot}5, \quad \text{where} \quad 50 < y_r^+ < 70. \tag{34}$$

Alternative assumptions to overcome some of the undesirable consequences of this assumption will be discussed later.

The pressure gradient term has been set equal to zero and the influence of this parameter as it is imposed by the outer region is considered later in greater detail.

The mean wall shear stress calculated with $\bar{T}_b u_\infty/\delta = 5$ and $u_0^+(y) = 16$ agrees reasonably well with empirical data in the range of Reynolds number considered (curve A of figure 10). The calculated values are scaled on ρu_*^2 derived from equation (33), which implies that the curves in figure 10 have to be compared with the line $\bar{\tau}_m/\rho u_*^2 = 1$. Curve B is the result for $\bar{T}_b u_\infty/\delta = 2{\cdot}5$ and is about 30 % too large when compared with the accepted value at $R = 3000$. The Einstein–Li result for $\bar{T}_b u_\infty/\delta = 5$ is given by C. The difference between A and C is what one would expect with the Rayleigh and Prandtl formulations for the skin friction for flow over a flat plate.

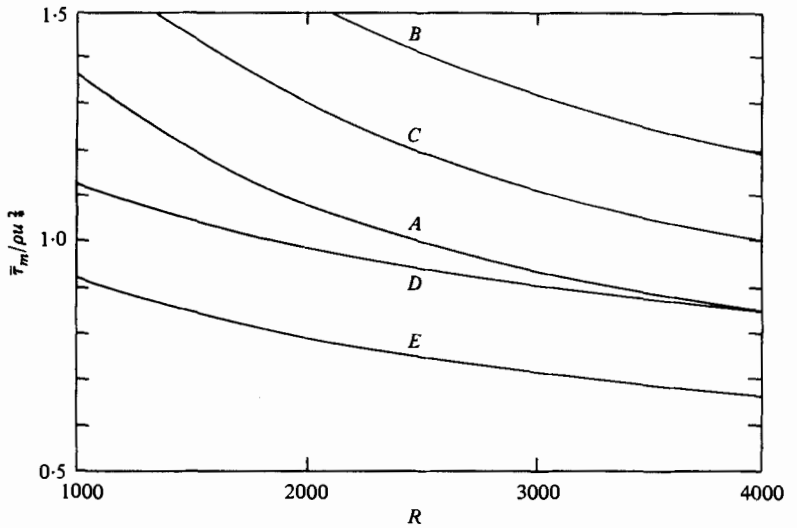

FIGURE 10. The mean wall shear stress $\bar{\tau}_m$, calculated with the two-dimensional model as function of the Reynolds number. The calculated values are scaled on ρu_*^2 according to (33). Different values for the two dimensionless parameters $[u_\infty \bar{T}_b/\delta;\ (du_0^+/dy^+]_{y=0}]$ are used, namely $(5; \infty)$ for A, $(2{\cdot}5; \infty)$ for B, $(2{\cdot}5; 1{\cdot}7)$ for D and $(5; 1{\cdot}7)$ for E. Curve C corresponds to the original 'surface renewal' model by Einstein & Li (1956).

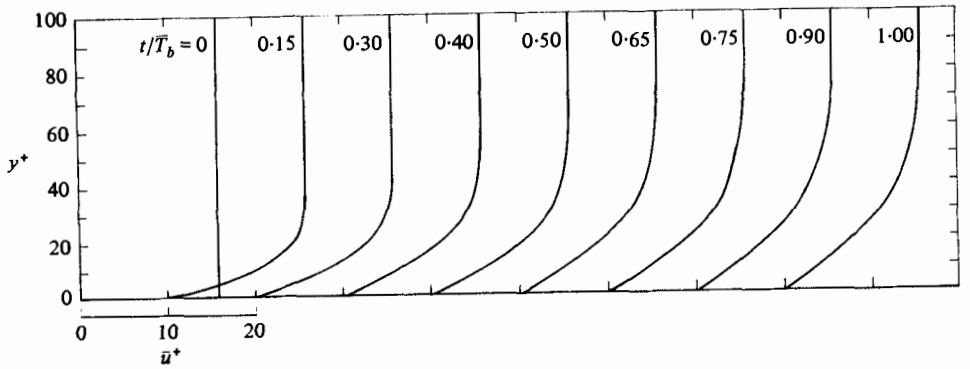

FIGURE 11. The time-dependent profiles as calculated from the two-dimensional model.

The uniform initial profile assumed by Einstein & Li leads to an infinite shear stress immediately after the passage of a burst. This is in conflict with the measurements of Eckelmann (1974) which indicate that the local wall shear stress rarely exceeds $1{\cdot}7\rho u_*^2$. A profile satisfying this condition and with a free-stream velocity corresponding to the Einstein–Li hypothesis, i.e. $u_0^+(\infty) = 16$, is chosen. The actual profile has been obtained by integrating the Blasius equation with a uniform initial profile ($u_0^+(y) = 16$) to a station where the skin friction equals the Eckelmann value. The resulting wall shear stress for the two burst periods is shown by curves D and E in figure 10. Curve D, corresponding to $\bar{T}_b u_\infty/\delta = 2{\cdot}5$, lies in the neighbourhood of 1, thus supporting the explanation for this choice of mean burst interval. The Reynolds number dependence for this choice of initial profile is weaker than the one exhibited for the uniform initial profile.

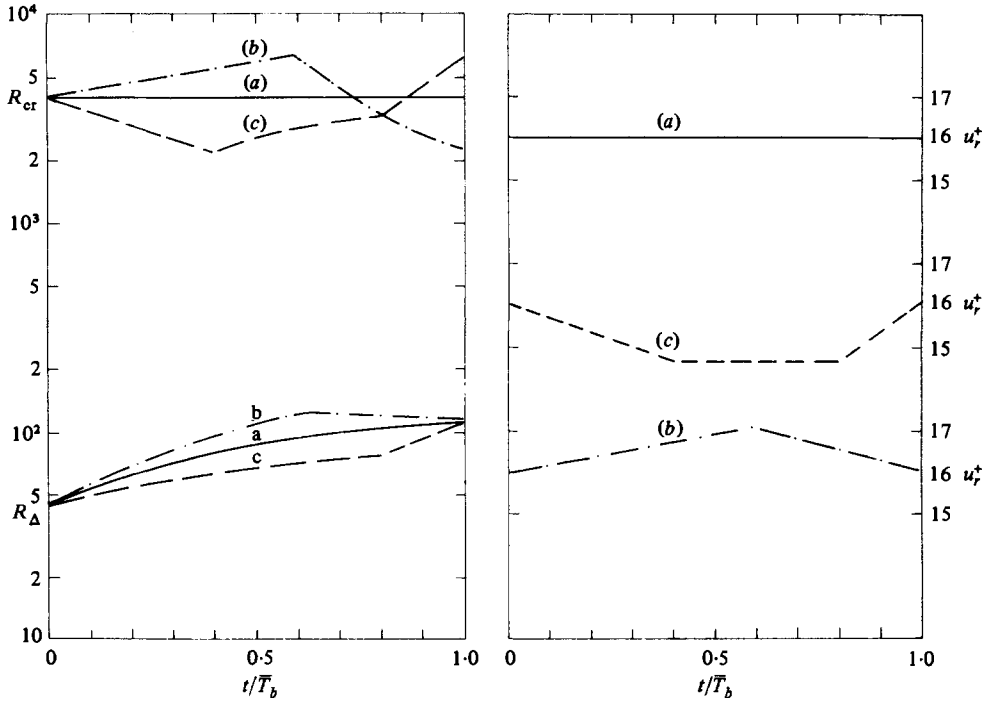

FIGURE 12. The critical Reynolds number R_{cr} and the actual Reynolds number R_Δ at different stages of development of the wall layer expressed by $t/\bar{T}_b$ (left figure). The different curves (*a*), (*b*) and (*c*) correspond to different boundary conditions outside the wall layer, given in the right-hand figure.

Figure 11 shows the time-dependent profiles at different stages of development of the wall layer. These profiles show a serious shortcoming of the present model. It is unable to predict an inflectional profile at the end of the period, which is believed to be the source of the local instability. To assist in further work, it is advantageous to estimate the critical Reynolds number associated with the local velocity profiles. Such an estimate can be arrived at from the plot of critical Reynolds number against shape factor (= displacement thickness/momentum thickness) presented by Shen (1964). This information has been used to arrive at plots shown in figure 12. For the present problem, the results are given by the curves labelled (*a*). The right-hand plots show the pressure distribution on the wall layer while the left-hand plots correspond to the critical Reynolds numbers, based on the momentum loss thickness of the viscous wall layer. It is clear from these plots that the profiles of figures 11 are highly stable; the critical Reynolds numbers are about two orders of magnitude larger than the prevailing local Reynolds number.

The foregoing discussion shows that the model does not incorporate mechanisms that are responsible for the development of unstable profiles. Two mechanisms are possible. (*a*) The local pressure gradient imposed by the outer region on the wall layer destabilizes the velocity profile. (*b*) Counter-rotating longitudinal vortices of the type discussed in § 2 above create inflectional zones in regions where the secondary motion is outwards.

The influence of pressure gradients is shown in figure 12. Curve (*b*) on the right-hand

plot is obtained from the measurements of Willmarth (1975*a*) while curve (*c*) corresponds to the results of Blackwelder & Kaplan (1972). The stability properties of profiles calculated with these pressure distributions depicted on the left-hand plots of figure 12 do not show any dramatic departure from the results described earlier. In other words the imposed pressure gradients have very little direct influence in creating locally unstable zones.

We now turn to the question of the second mechanism proposed above. The experimentally observed periodicity in the z direction has been attributed to the counter-rotating vortices with their axes in the longitudinal direction (Blackwelder & Eckelmann 1979). Since the information on the appropriate form of boundary conditions to be used in the spanwise direction is rather scant, no attempt has been made to solve a fully three-dimensional wall layer. Instead the w-component of the velocity vector is treated as a known quantity and provides a source term in the governing equations. The equations for the wall layer are modified as

$$\tilde{u}_c\frac{\partial\tilde{u}_c}{\partial x_c}+\tilde{v}_c\frac{\partial\tilde{u}_c}{\partial y_c}+\tilde{w}_c\frac{\partial\tilde{u}_c}{\partial z_c}=u_{cr}\frac{\partial u_{cr}}{\partial x_c}+\nu\frac{\partial^2\tilde{u}_c}{\partial y_c^2}+\nu\frac{\partial^2\tilde{u}_c}{\partial z_c^2}, \tag{35}$$

$$\frac{\partial\tilde{u}_c}{\partial x_c}+\frac{\partial\tilde{v}_c}{\partial y_c}+\frac{\partial\tilde{w}_c}{\partial z_c}=0. \tag{36}$$

The $\tilde{w}_c$ component is assumed to be sufficiently small that it does not disturb the boundary-layer approximation nor does it interfere with the two-layer structure in the y_c direction. A $\tilde{w}_c$ profile similar to the one used by Stuart (1965) in his studies on the effect of longitudinal vortices on the transition process has been adopted in this investigation:

$$\tilde{w}_c^+\equiv\frac{\tilde{w}_c}{u_*}=\phi(y^+)\sin\frac{2\pi z^+}{\lambda_z^+} \tag{37}$$

where $\phi(y^+)=\beta\gamma[-\exp(-\gamma y^+)+4\exp(-2\gamma y^+)-3\exp(-3\gamma y^+)]$.

The quantity λ_z^+, usually called streak spacing, is taken equal to 100 – a value supported by measurements of Kline *et al.* (1967), Bakewell & Lumley (1967) and Gupta, Laufer & Kaplan (1971).

Optimal values of β and γ, representing the strength and the y-scale of the vortices, are found on the basis of numerical experimentation. γ is chosen to provide a horizontal shear layer at the end of the period at $y^+\simeq 30$. β is adjusted so that an unstable profile results at the end of the period. The values so obtained are $\beta=20$ and $\gamma=0{\cdot}06$. The resulting velocity profiles are shown in figure 13. At $z^+=50$, where the secondary motion is outward, the profiles show clearly an inflection point towards the end of the period. A more dramatic representation of the effect of the counter-rotating vortices on the stability properties of the wall layer is shown in figure 14, which compares the critical Reynolds number with the actual Reynolds number. The effect of the strength of these vortices, i.e. β, on $t/\overline{T}_b$ where $R_\Delta=R_{cr}$, is set out in table 2, showing the rather strong influence of this parameter on stability. Figure 15 compares the mean wall shear stress obtained with the present model and curve *D* of figure 10. The counter-rotating vortices increase the shear stress only slightly when compared with the earlier result and reduce the Reynolds-number dependence somewhat.

The mean velocity profiles calculated on the basis of the different models are in reasonable agreement with experimental results (see Beljaars 1978).

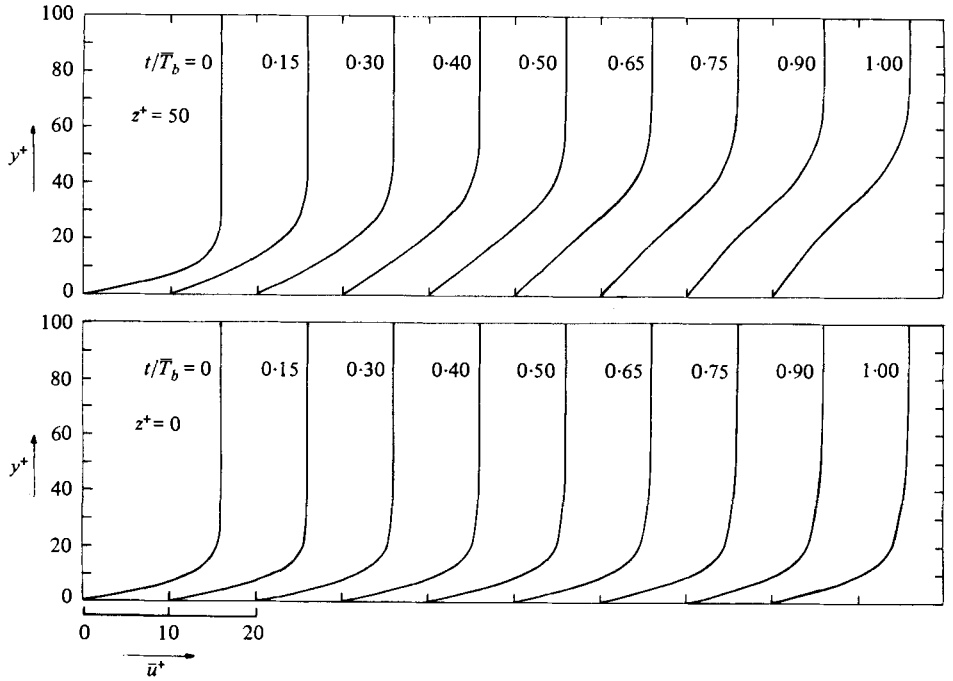

FIGURE 13. Time-dependent profiles, calculated with the three-dimensional model.

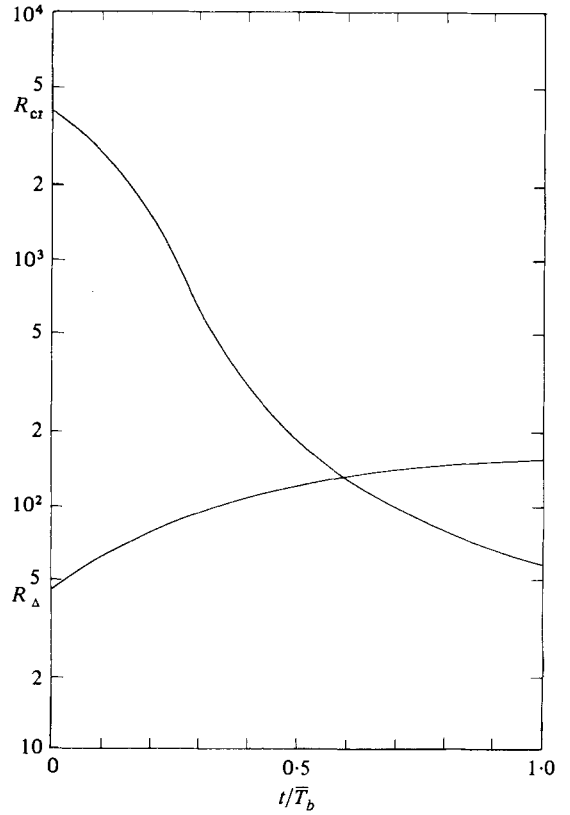

FIGURE 14. The critical Reynolds number compared with the actual Reynolds number for the three-dimensional model as a function of the stage of development of the wall layer at $z^+ = 50$.

β	$(t/\bar{T}_b)_{R_\Delta = R_{cr}}$	$\bar{\tau}_m/\rho u_*^2$
0	1400	0·904
10	1·40	0·933
15	0·81	0·968
20	0·61	1·008
25	0·48	1·065
30	0·39	1·121

TABLE 2. The value of $t/\bar{T}_b$, where $R_\Delta = R_{cr}$, and the mean wall shear stress for different values of β; $Re = 3000$.

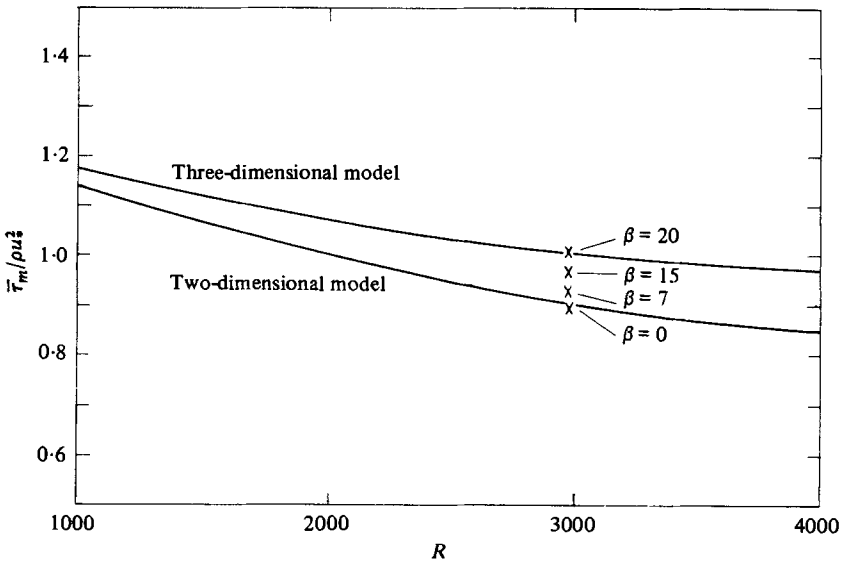

FIGURE 15. The influence of the counter-rotating vortices on the predicted mean wall shear stress. $u_\infty \bar{T}_b/\delta = 2{\cdot}5$; $(du_0^+/dy^+)_{y=0} = 1{\cdot}7$; $\gamma = 0{\cdot}06$.

The model described so far is purely deterministic, but the input parameters the model employs are known to be stochastic variables. Rao, Narasimha & Badri Narayanan (1971) and Kim *et al.* (1971) suggest a lognormal distribution function for $\bar{T}_b$. Application of this distribution function to average over a number of periods increased the mean wall shear stress only by about 3%. Little is known about the statistical properties of other parameters; a sensitivity check on the results by changing these parameters showed no significant influence on the mean wall shear stress (see Beljaars 1979 for details).

Lastly, we turn to the influence of imposed pressure gradients on the stability properties of the three-dimensional model. The results are summarized in figure 16. Curves (*a*), (*b*) and (*f*) correspond to the same conditions as in figure 12. While the pressure gradient does influence the stability of the wall layer, this influence is not nearly as strong as that corresponding to varying β (see table 2).

An important question in this connection is the possible mechanism of synchronization of structures in the wall layer with those in the outer layer. If the burst events are initiated by the local pressure gradient, as suggested by Nychas, Hershey & Brodkey

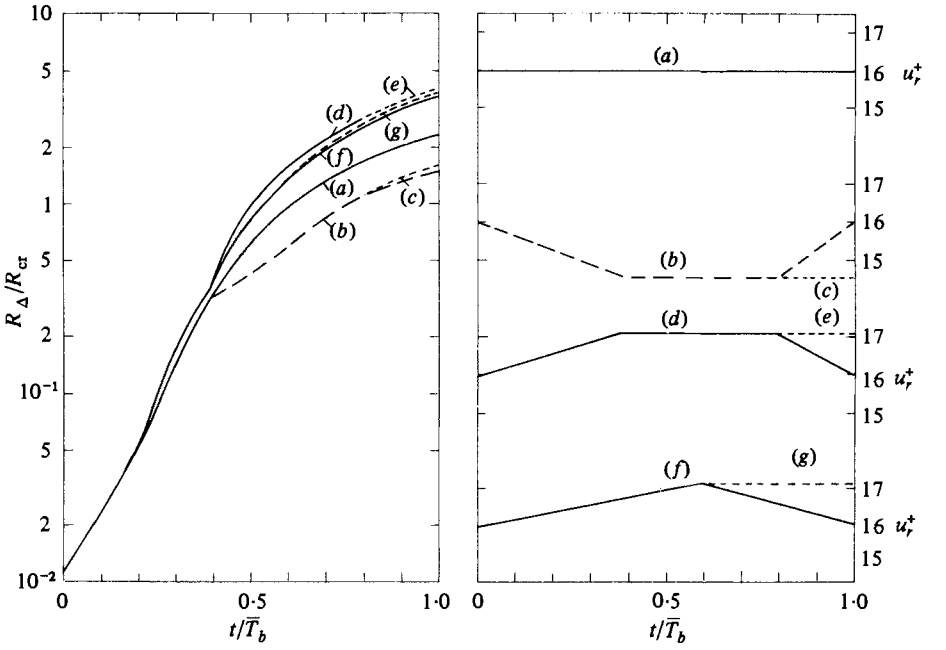

FIGURE 16. The actual Reynolds number R_Δ divided by the critical Reynolds number R_{cr} as a function of the stage of development $t/\bar{T}_b$ (left-hand figure). The different curves correspond to different upper boundary conditions u_r^+ as indicated in the right-hand part of the figure.

(1973), then a sudden increase or decrease of u_r^+ at the end of a cycle should have a considerable influence on the stability of the resulting profile. A comparison of the stability of profiles obtained with conditions (*c*), (*e*) and (*g*) (shown on the right-hand side of figure 16) shows a negligible difference from those obtained with (*b*), (*d*) and (*f*). The results presented here strongly suggest that the synchronization is to be achieved through the agency of the counter-rotating vortex strength, β. We shall return to this point in the final section.

5.2. *Outer-layer results*

The parameters that need specification before numerical results can be obtained from the discrete vortex approximation are: the initial conditions for the jet (X_{bc0}, u_{bc0}, v_{bc0}), the surface area of the jet S, the coefficients c_x and c_y determining the friction between the ejected and surrounding fluid, and the initial distribution of the point vortices.

The initial conditions for the ejection jets are deduced from the wall layer calculations. Application of continuity arguments to a control volume around the burst region (see figure 17) results in

$$Sv_{bc0} = \int_0^\infty \int_0^{\lambda_z} [u_1(y) - u_0(y)]\, dy\, dz. \tag{38}$$

The choice of u_{bc0} is based on the idea that the contribution of the ejected jet to the shear stress, when smeared out over one period in the x and z directions, is equal to the wall shear stress. Thus

$$\frac{Sv_{bc0}}{\lambda_x \lambda_z}[u_{bc0} - \tilde{u}_c(X_{bc0}, 0)] = u_*^2, \tag{39}$$

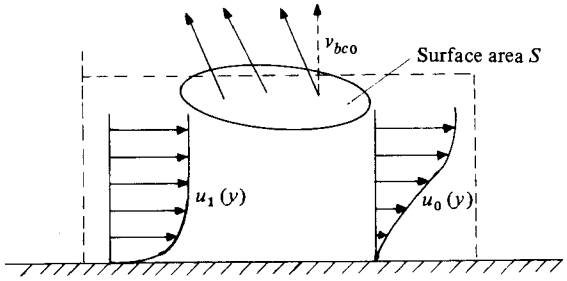

FIGURE 17. Conservation of mass in the burst region.

where $\tilde{u}_c(X_{bc0}, 0)$ is the velocity induced by the discrete vortices. v_{bc0} is estimated by noting that $u'v'$ is observed to have a peak value of about $20u_*^2$, so that

$$v_{bc0} = 20\frac{u_*^2}{u_{bc0} - \tilde{u}_c(X_{bc0}, 0)}. \tag{40}$$

X_{bc0}, to conform with the proposed synchronization mechanism, should be located at the point where a maximum of $\tilde{u}_c(X_{bc}, 0)$ occurs. Because of the numerical 'noise' produced by the discrete-vortex approximation, it was impossible to find a reliable velocity maximum near the wall. Therefore X_{bc0} was taken as a constant, assuming that the large-scale structures are stationary in the moving frame.

Very little information is available for the choice of c_x and c_y. Small c_x results in large times for the ejected jets to lose their identity, and for small c_y the jets will penetrate to large distances from the wall. The following approximations to equations (29) have been used to obtain the actual values. Neglecting $\tilde{v}_c$ in the second of equations (29) as small close to the wall, the solution can be written as

$$\left.\begin{aligned} v_{bc} &= v_{bc0}\exp\left[-c_y(t-t_0)\right], \\ Y_{bc} &= \frac{v_{bc0}}{c_y}\left[1-\exp\left(-c_y(t-t_0)\right)\right]. \end{aligned}\right\} \tag{41}$$

In this approximation v_{bc0}/c_y is the maximum distance that the jet can penetrate. Taking $Y_{bc} = \delta$, we obtain c_y.

Using the second of equations (41), the first of equations (29) can be transformed into the Y_{bc} co-ordinate. The resulting equation is

$$\frac{d(u_{bc}-\tilde{u}_c)}{dY_{bc}} = -\frac{c_x(u_{bc}-\tilde{u}_c)}{v_{bc0}-c_y Y_{bc}} - \frac{d\tilde{u}_c}{dY_{bc}}. \tag{42}$$

The quantity, $(u_{bc}-\tilde{u}_c)$, representing the small-scale velocity fluctuation, is proportional, for small Y_{bc}, to the small-scale Reynolds stress. Since shear stress can be expected to be nearly constant in the neighbourhood of the wall, the left-hand side of equation (38) can be set to zero, thus leading to

$$c_x = -v_{bc0}\left(\frac{d\tilde{u}_c/dY_{bc}}{u_{bc}-\tilde{u}_c}\right)_{(X_{bc0},\,0)}.$$

The model developed above cannot be very accurate. However, it duplicates the

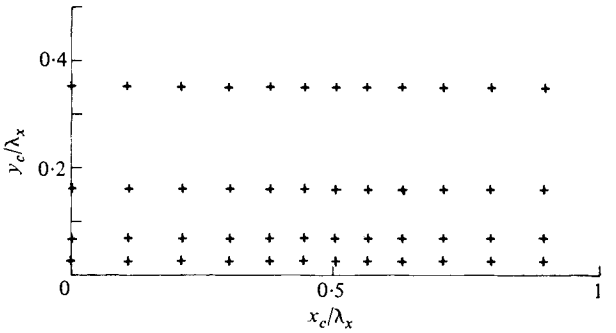

FIGURE 18. Vorticity distribution from which the initial condition has been derived.

characteristic feature of localized momentum exchange of the burst event near the wall – a feature which is believed to be important.

The initial condition for the vortex distribution is generated by the following procedure. The vorticity distribution corresponding to a $\frac{1}{7}$ power law is discretized by concentrating the vorticity in four layers. A non-uniform distribution in the x direction is chosen to avoid the vortices following a completely regular pattern (see figure 18). This distribution is smoothed out in the y direction by integrating the first of equations (23) from $t = 0$ to $t = 6\lambda_x/u_\infty$. The resulting vortex distribution has been chosen as the initial condition for all the calculations presented here. It should be pointed out that the distribution thus constructed does not represent all the vorticity of the turbulent boundary layer. The vorticity near the wall has been ignored, as the corresponding vortex elements will be too close to their image elements, resulting in no influence on the velocity field far from the wall. Thus the development of structures with dimensions of boundary-layer thickness in the y direction will not be influenced by this artifice.

The calculations presented here provide the evolution of the large-scale field for several wavelengths of the turbulent boundary layer on its way downstream. To determine the influence, or otherwise, of the burst events on the large-scale structures in the outer region, the time evolution of the latter is calculated with and without the 'ejection jets'. The results are given in figures 19 and 20 in the form of vortex positions at different times as well as instantaneous streamlines. Only one wavelength is represented in the calculation field. The streamlines have been determined by interpolation among stream functions at the modal points of a 10×10 grid. The moving-frame representation in the figure corresponds to downstream evolution of structures in the laboratory co-ordinates. The value of λ_x is held constant for the entire period of computation.

Vorticity, in the absence of burst events, tends to be uniformly distributed over the x axis with only weak vorticity concentrations (figure 19). Preliminary calculations with strong vorticity concentrations in the initial condition (surrounded by several streamlines) showed that the vorticity concentrations disappeared after a certain time. The characteristic time for eddies to lose their identity is of the order of $7\lambda_x/u_\infty$.

The stream-function contours of figure 20, representing the calculations with the burst events included, show a behaviour different from that of figure 19. The trajectory of the ejected fluid is indicated by the dashed line. The ejected fluid leaves the wall region at $x_c/\lambda_x = -0{\cdot}2$, but also at 0·8 because of the periodicity. The contours clearly

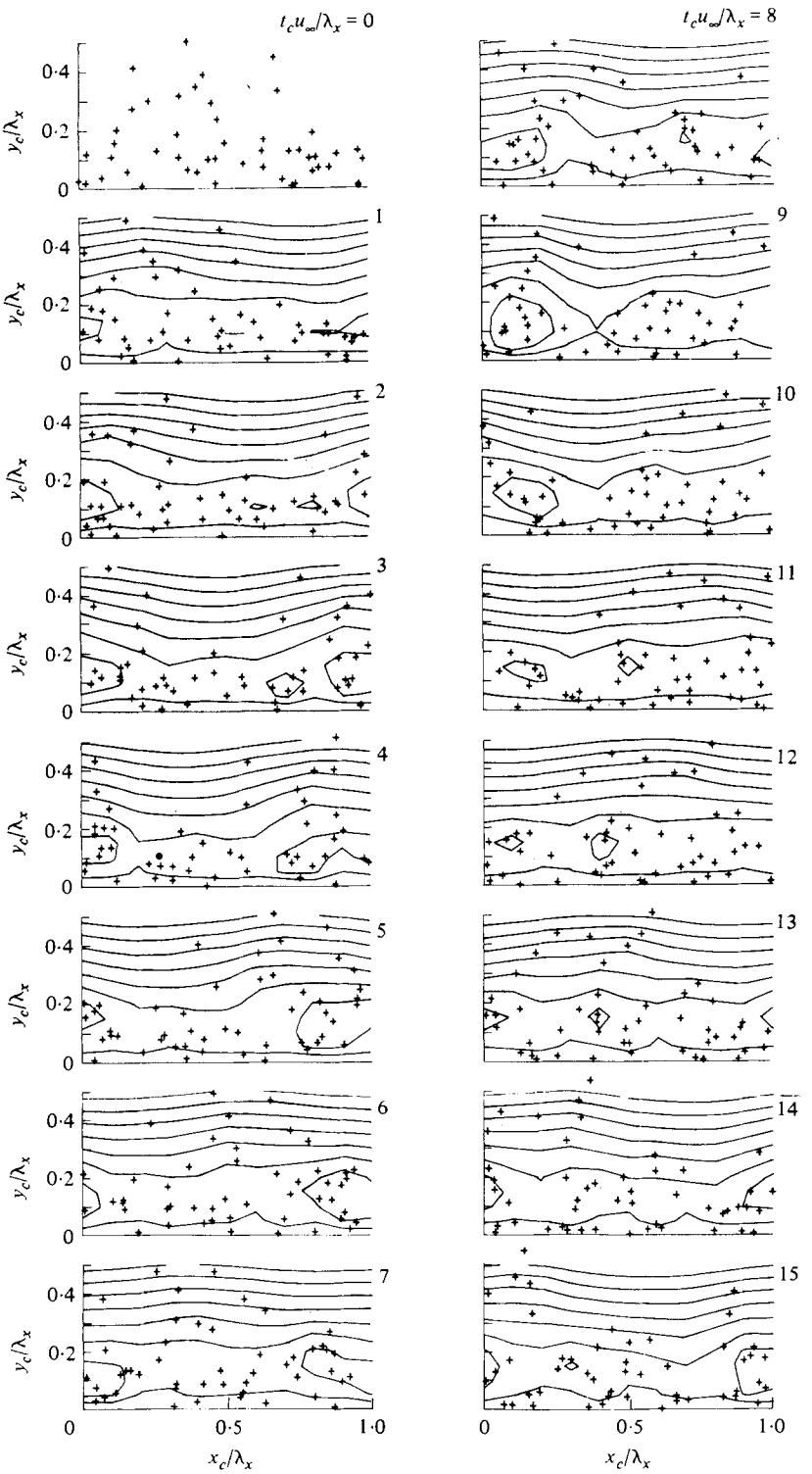

FIGURE 19. Stream-function contours and vortex positions (+) at different times. The effect of the burst events has not been included.

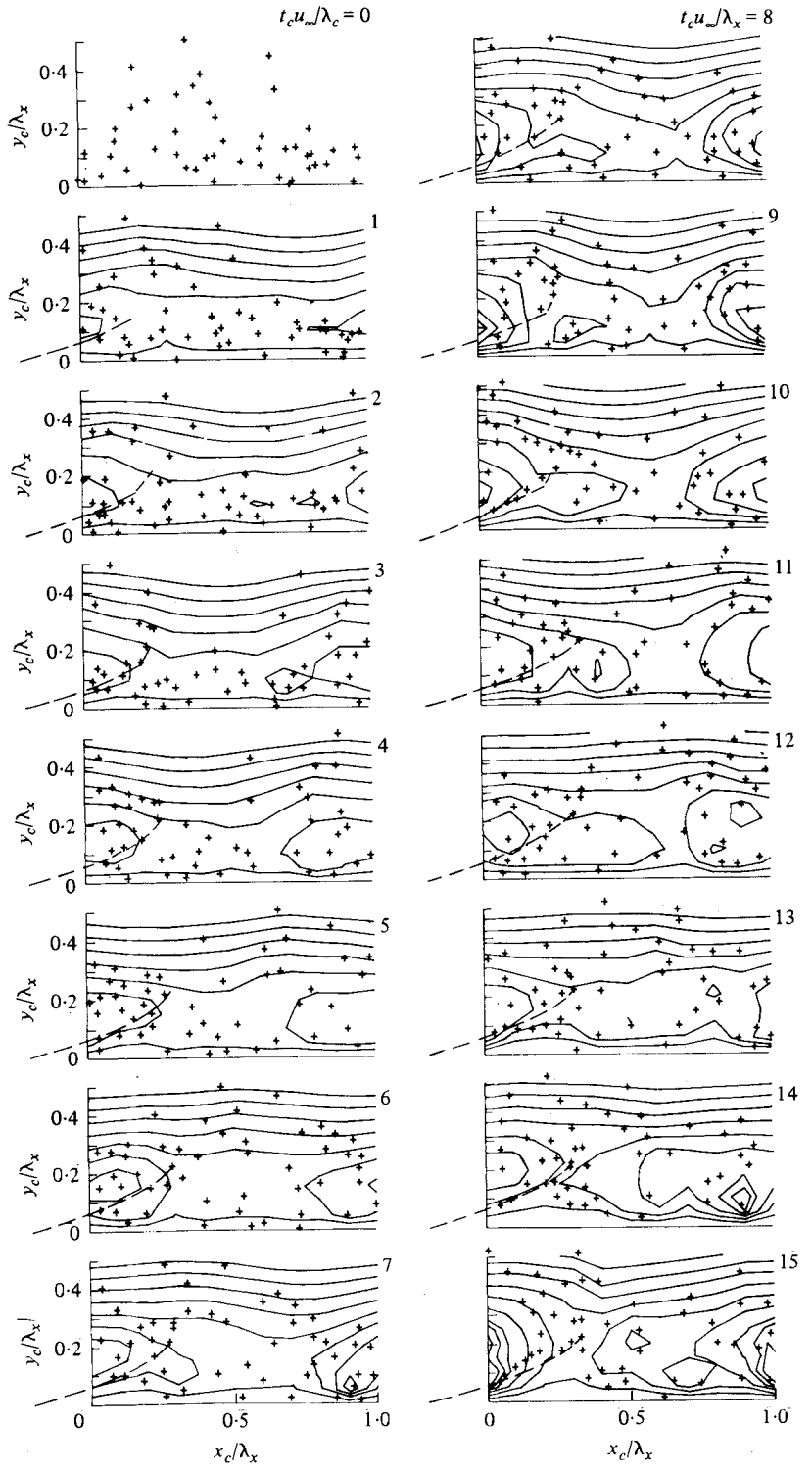

FIGURE 20. Stream-function contours and vortex positions (+) at different times. The dashed lines represent the trajectories of the fluid ejected in a burst.

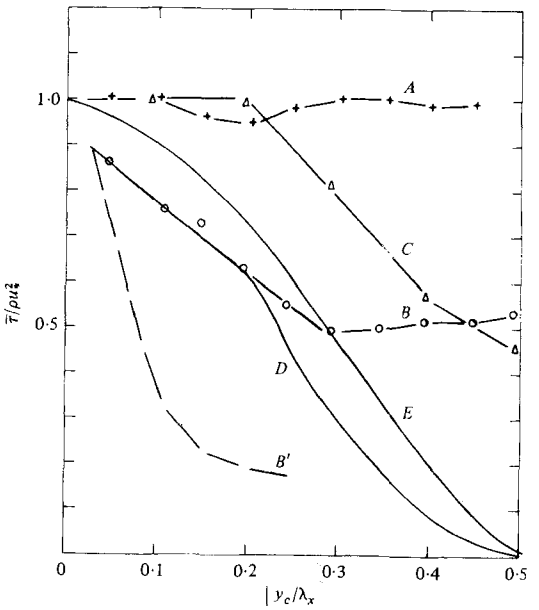

FIGURE 21. Shear stress profiles calculated for three different cases: outer-layer calculation without burst events (A), with burst events (B) and with vortex pairing (C). The dashed line indicates the contribution to the shear stress of the 'ejection jets' only. $y_c/\lambda_x = 0{\cdot}5$ corresponds to the edge of the boundary layers. D is a composite of B and C, while E corresponds to Coles' law of the wake.

show the formation of new vorticity concentrations under the influence of the burst events, which generate small amounts of vorticity locally. This vorticity build-up is more pronounced than in the previous case, where the picture is more stationary.

In both cases discussed above, there are fluctuations that look like random ones. These never result in any strong vorticity concentrations. These fluctuations have a period of the order of $7{\cdot}5\lambda_x/u_\infty$. In this period, the moving frame translates 12 boundary-layer thicknesses downstream – a distance that corresponds to the characteristic correlation distance found experimentally by Blackwelder & Kovasznay (1972). This time appears to be characteristic of the large-scale motion and is unaltered by the presence of bursts.

We next turn to the question: which eddies are responsible for the turbulent stress? This stress is essentially equal to the product of u and v fluctuations and can easily be calculated from the time-dependent data. Unfortunately, the small number of vortices in the field causes large velocity fluctuations, that do not contribute to the turbulent stress, but make the direct turbulent stress calculations very inaccurate. It turned out to be more accurate to derive the turbulent stress from the time evolution of the mean profile. We know that

$$\frac{1}{\rho}(\tau-\tau_w) = \frac{1}{U_c}\frac{\partial}{\partial t_c}\int_0^{y_c}(U_c-\tilde{u}_c)^2\,dy_c - \frac{U_c-\tilde{u}_c}{U_c}\frac{\partial}{\partial t_c}\int_0^{y_c}(U_c-\tilde{u}_c)\,dy_c, \tag{43}$$

where τ is the local shear stress at distance y_c from the wall. The integration constant τ_w is chosen to be the wall shear stress. Equation (43) is averaged to obtain the mean shear stress. The $\tilde{u}_c$ profiles are averages over one wavelength and a certain time. The

average $\tilde{u}_c$ over the time interval $(7{\cdot}5\lambda_x/u_\infty)$ is taken to be the mean profile at $3{\cdot}75\lambda_x/u_\infty$. Similarly the mean profile at $11{\cdot}25\lambda_x/u_\infty$ is obtained. The time derivative is approximated from these two profiles. The resulting shear stress profiles are shown in figure 21.

Curve A shows the shear stress in the absence of bursts, and it is seen to be a constant which is simply the integration constant in equation (43). This implies that the mean streamlines are parallel to the wall, thus showing no boundary-layer growth. When burst events are incorporated, the shear stress decreases to half the wall shear stress at approximately half the boundary-layer thickness (curve B). Curve B' shows the part that is contributed by the small-scale events. The difference must be attributed to the large-scale time-dependent movement itself. It is remarkable that the large-scale movement transports momentum in the presence of ejection jets. The ejection jets contribute substantially to the momentum transport in a relatively thin layer near the wall; further away from the wall, the large-scale eddies take over the transport. Probably it is the incorporating of low-momentum fluid at the bottom of these large-scale eddies that makes them effective. Without this mechanism, they revolve, but do not transport momentum.

The calculations presented above do not go far enough; the shear stress profile levels off at half the boundary-layer thickness. Apparently, we are still missing a transport mechanism. In the calculations up to this point λ_x has been held constant; since λ_x scales on the boundary-layer thickness, δ, these calculations do not provide for the growth of the boundary layer. The growth of the x wavelength can be simulated in the present model by admitting interaction between two or more structures with scale λ_x. This process is investigated by taking two wavelengths λ_x in one calculation interval and by perturbing the field of one wavelength with respect to that in the other. Such a perturbation can easily arise, for example, from a change in the burst interval time. The two periods are identical at $t_c = 0$ except that all the vortex elements in the second one are shifted by $0{\cdot}06\lambda_x$ in the positive y_c direction. The results are shown in figure 22. Since the two structures have slightly different distances from the wall, they have different convection velocities. Hence the right vortex structure passes over the left one and, during the process, the upper structure absorbs vorticity from the lower one. When they separate again at $t_c \simeq 12\lambda_x/u_\infty$ the lower one is much less pronounced than the upper one. Although the process is not identical, there is a strong resemblance to vortex pairing observed in mixing layers. This process might be responsible for the scale increase of structures on their way downstream. Such a process must exist, since the boundary layer thickens and the large eddies scale on the boundary-layer thickness.

The corresponding shear stresses are shown as curve C in figure 21. Now the shear stress gradient appears only in the outer part, but not in the inner part. It is difficult to incorporate the burst mechanism into these calculations, since it is to start in two periods and then to merge into one period. But it is not impossible that the different mechanisms complement each other in forming a shear stress profile from (*a*) the burst events in a thin layer near the wall; (*b*) the large-scale structures in the inner half of the boundary layer; and (*c*) the vortex pairing in the outer half of the boundary layer.

With the last comment, (*c*), in mind, a composite shear stress profile was constructed from the profiles B and C by subtracting the common constant τ_w to avoid the double counting. Such an additive composition, while strictly not justifiable, is plausible

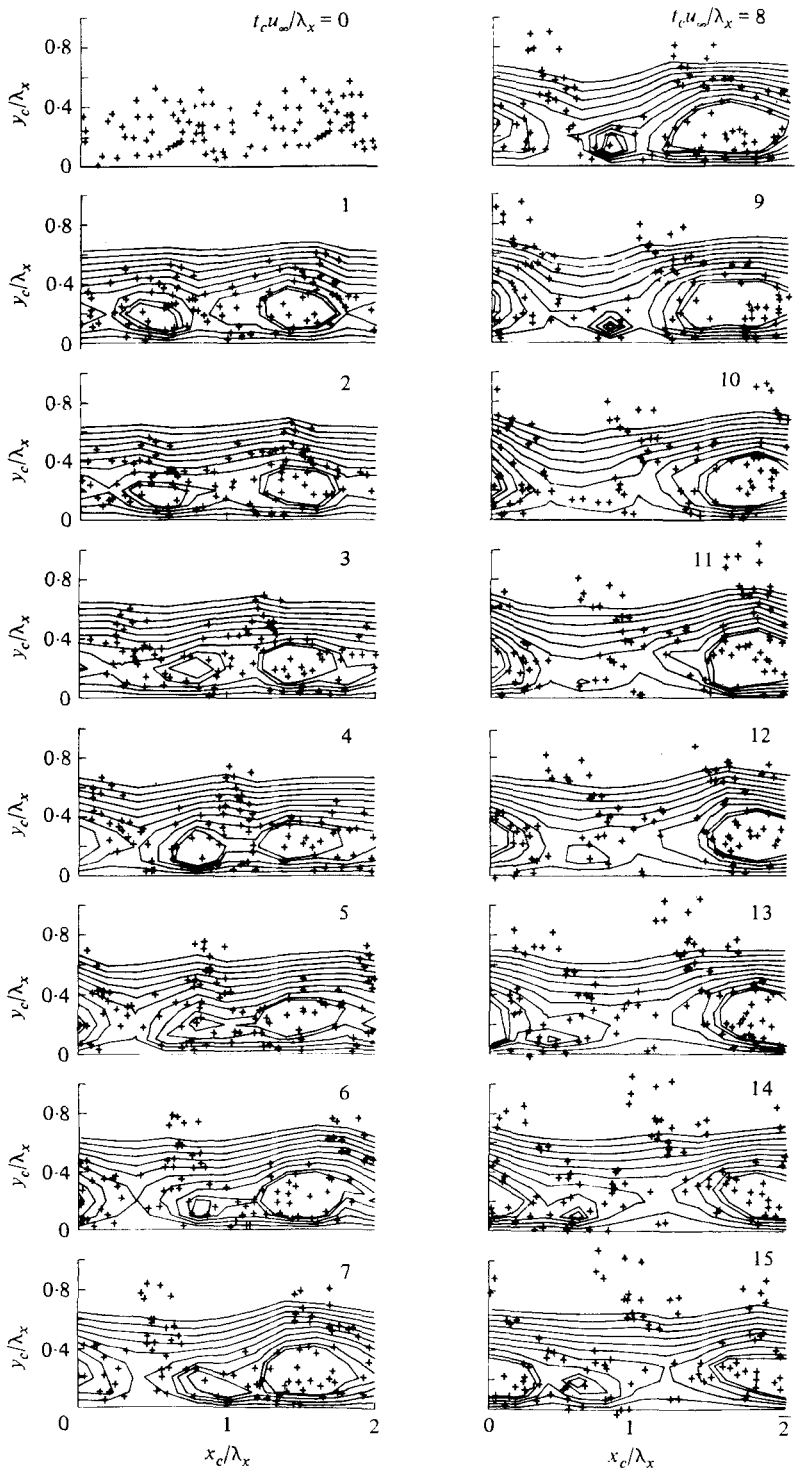

FIGURE 22. Illustration of the interaction between two vortex structures: vortex pairing. The calculation field includes two wavelengths λ_x.

because the ejection jet interaction mechanism assumes the constants relevant to a region near the wall while the structure interaction mechanism is relevant only far away from the wall. Be that as it may, it is remarkable that the resulting shear stress profile, D, bears a striking resemblance to curve E, obtained from Coles' law of the wake (Hinze 1975). Considering the rather crude assumptions employed in arriving at the numerical results, the quantitative agreement could be thought of as acceptable. The authors have resisted the temptation to bridge the gap between D and E by adjusting the half-a-dozen or so constants at their disposal. While this may be necessary in the ultimate analysis, it should await further work with the model.

Before concluding this section, it is worth while to make another observation. Motion pictures were made out of the computer graphics with marker lines in the flow field. An examination of these demonstrated clearly the phenomenon of intermittency at the edge of the boundary layer, as also of entrainment. In fact, when the marker line was located at $0{\cdot}8\delta$ from the wall, it almost reached the wall. Because of difficulties of reproducing these figures, they have not been included here.

6. Concluding remarks

The relatively simple deterministic model described in the paper is able to explain many of the observed features of the turbulent boundary layer. In particular, the wall shear stress is well predicted and mechanisms that are responsible for momentum transfer in the outer region are clarified by the numerical results. These results show the importance of coherent motions for the transport process in a turbulent boundary layer.

The counter-rotating vortices in the wall layer have only a marginal influence on the wall shear stress. On the other hand they play a decisive role in creating unstable conditions, thus providing for periodic regeneration of bursts. Although the existence of the counter-rotating vortices seems to be well established now, the mechanism that causes them is not yet clear. Several authors (cf. Brown & Thomas 1977) refer to the Taylor–Görtler type of instability, which is usually observed in boundary-layer flows along concave walls. The present results support this idea.

In the wall region of the present model, curvature of streamlines arises because of the growth of the wall layer as well as because of the pressure gradient imposed by the outer region. The fact that a very small curvature of the streamlines is sufficient for the onset of a Taylor–Görtler instability mode has been demonstrated by Witting (1958). This work perturbs a parallel Blasius boundary layer with a small-amplitude Tollmien–Schlichting wave. It is shown that as little an increase in the wave amplitude as $10^{-4}\delta_m$ is sufficient to trigger this mode of instability. More recently Brown & Thomas (1977) have produced dimensional arguments to suggest that conditions are appropriate in the vicinity of the wall for the onset of this mode of instability.

Another important effect of the counter-rotating vortices is that they shift the occurrence of a succeeding burst by $\frac{1}{2}\lambda_z^+$ in the spanwise direction. Experimental observation of Offen & Kline (1974, 1975), discussed in §2, confirms this finding. Moreover, it justifies the explanation provided there for the existence of a single period for inner and outer structures as against the rather widely held opinion that a factor of 2 relates the periods in the inner and outer structures.

A vexing question is the synchronization mechanism that keeps the inner and outer

regions in step. That they are synchronized can hardly be doubted, particularly in the face of evidence that the mean burst interval scales on outer-layer parameters. The results of this investigation show that the pressure gradient cannot directly achieve this task. The most obvious candidate is the strength of the longitudinal vortices, β, which is shown to have a very strong influence on the stability of the wall layer. Accordingly, one would expect that β would increase towards the end of the period. Such a situation would be consistent with the observations of Kline *et al.* (1967) and Corino & Brodkey (1969), which indicate that the burst event is preceded by a sudden increase in the thickness of the retarded layer – the so-called lift-up. The continued interaction of the pressure gradient with the longitudinal vortices (once they are set up) by means of the Taylor–Görtler instability mechanism would indeed be consistent with an increase of u_r^+ (the free-stream velocity imposed on the wall layer) at the end of the cycle, since such an acceleration would cause a more pronounced concavity of the streamlines.

We now turn to the results from the outer-layer calculations. A remarkable result of these calculations is that the large-scale structures contribute to the Reynolds stress *only* in the presence of small-scale effects in the form of burst events, even though the latter are highly localized occurrences. The burst events thus form an essential coupling between the wall and outer regions. The increase of scale of outer structures in the downstream direction and the creation of Reynolds stress in the outermost part of the boundary layer is possibly caused by a phenomenon of vortex amalgamation that resembles vortex pairing in mixing layers. Thus the significant outcome of these calculations is that *individual structures acting by themselves are incapable of transporting momentum.* They need to interact with other structures – be these from the wall region (ejection jets) or neighbouring structures in the outer region but with slightly different characteristics.

An important question in this context is the justification for treating the outer structures as two-dimensional. Experiments show the presence of three-dimensional turbulence of different scales. The present results suggest, however, that the two-dimensional part of the turbulence dominates the transport process. We conclude from this that the motion in the third direction plays a relatively minor role in determining momentum transport. This situation is widely accepted for the fine-grained turbulence that comes down the energy cascade and is almost isotropic. The latter has been completely ignored in the present model as irrelevant for the transport process.

A comparable situation exists for the mixing layer; although the observed turbulence is clearly three-dimensional at high Reynolds numbers, the two-dimensional eddies still dominate the mixing-layer growth and the Reynolds shear stress (Brown & Roshko 1974). Moreover, the two-dimensional eddy simulation of this problem by Acton (1976) turns out to be quite successful.

Whether a similar situation exists in the boundary layer cannot be definitively concluded at this moment. Experiments on this score are ambiguous. Some experimental studies emphasize the large-scale structures that rotate in the x, y plane (Brown & Thomas 1977; Kovasznay *et al.* 1970). Head & Bandyopadhyay (1979) concentrate on the complex three-dimensional structures. The latter study, however, indicates that a majority of these three-dimensional structures do not survive until the outer regions of the boundary layer. This in particular could be taken to mean that these structures have their origin in the wall region. It is worth while to recall here a result

of the present calculations: the contribution of the wall region structures to the Reynolds shear stress in the outer layer is limited to a narrow region close to the wall; at the most this region covers about 20 % of the boundary layer. In any event, none of the experiments cited above investigates the contribution of the observed structures to the Reynolds shear stress. A clear conclusion of the present study is that the two-dimensional eddy transport in the outer region is not in conflict with the basic equations of motion.

The model proposed in the present work is purely deterministic; however, a certain amount of the stochastic nature can easily be built into it by the use of fluctuating parameters. These fluctuations cannot be expected to change either the dynamics or the transport properties of structures in the wall layer. The situation in the outer layer is not so certain; these fluctuations may be responsible for producing phase differences among structures which appear to be essential for the vortex amalgamation process described above. These fluctuations will certainly introduce randomness in the 'model turbulence'. In particular, when this randomness occurs in the scales of successive structures, it poses a formidable problem for conditional sampling experiments. It is not sufficient simply to isolate the structures, but necessary to identify the scales associated with them. When averaging is performed without taking this into account, considerable blurring of information will result, leading to spurious results about structures. Much of the arguments against coherent structures may perhaps be attributed to this problem.

Finally, it is interesting to compare the results of the present work with a few descriptive ideas about wall-bounded turbulent motions. Townsend (1961) introduced the concept of 'active' and 'inactive motions'. The large-scale eddies, in this concept, do not contribute to the Reynolds shear stress at distances from the wall that are small compared with the scale of these eddies; however, they contribute to the turbulence intensity at these positions. Such motions have been labelled inactive. The structures in the outer region of the present model show this behaviour and thus correspond to inactive motions. The burst events can be thought of as active motions in Townsend's scheme.

The process of vortex amalgamation in the boundary layer is much less pronounced than in the free mixing layer. This is probably the reason why it has never been observed in a boundary layer. The sudden outward movements observed by Kovasznay *et al.* (1970) may very well be related to this process. The amalgamation is a rather sudden event which can easily get lost in a welter of small-scale events.

Falco (1977) postulates what he calls 'typical eddies' as being responsible for the turbulent stress throughout the boundary layer. The observed typical eddies seem to originate in the wall layer; it is not clear whether they contribute to the turbulent stress in the outer part of the boundary layer. The present calculations do not support this contention.

Praturi & Brodkey (1978) conclude on the basis of their stereoscopic visual study that the burst events cover only a fraction of the boundary-layer thickness and two-dimensional vortex structures dominate the outer region – features that provide an important support for the present analysis. However, their interpretation of the mechanisms involved is at variance with the findings here. Praturi & Brodkey claim that the wall layer reacts to the outer region, but does not influence it. The longitudinal vortices in the wall layer are seen as a result of the spanwise periodicity and not as the

origin of it. Such simplistic cause-and-effect relationships are not supported by the present results. It has been shown that new bursts can occur only in the presence of longitudinal vortices which are presumed to be caused by the outer structures. The vortex structures retain their coherence only in the presence of burst events.

REFERENCES

ACTON, E. 1976 The modelling of large eddies in a two-dimensional shear layer. *J. Fluid Mech.* **76**, 561.

BELJAARS, A. C. M. 1978 A quantitative model for momentum exchange by coherent motions in a turbulent wall boundary layer. *Lett. Heat & Mass Transfer* **5**, 231.

BELJAARS, A. C. M. 1979 A model for turbulent exchange in boundary layers. Ph.D. thesis, Eindhoven University of Technology, Netherlands.

BAKEWELL, H. P. & LUMLEY, J. L. 1967 Viscous sublayer and adjacent wall region in turbulent pipe flow. *Phys. Fluids* **10**, 1880.

BARK, F. H. 1975 On the wave structure of the wall region of a turbulent boundary layer. *J. Fluid Mech.* **70**, 229.

BLACK, T. J. 1968 An analytical study of the measured wall pressure field under supersonic turbulent boundary layers. N.A.S.A. CR-888.

BLACKWELDER, R. F. & ECKELMANN, H. 1979 Streamwise vortices associated with the bursting phenomenon. *J. Fluid Mech.* **94**, 577.

BLACKWELDER, R. F. & KAPLAN, R. E. 1972 The intermittent structure of the wall region of a turbulent boundary layer. *Univ. S. Calif. Rep. USCAE*, 1–22.

BLACKWELDER, R. F. & KOVASZNAY, L. S. G. 1972 Time scales and correlation in a turbulent boundary layer. *Phys. Fluids* **15**, 1545.

BROWN, G. L. & ROSHKO, A. 1974 On density effects in turbulent mixing layers. *J. Fluid Mech.* **64**, 775.

BROWN, G. L. & THOMAS, A. S. W. 1977 Large structure in a turbulent boundary layer. *Phys. Fluids* Suppl. **20**, 243.

CEBECI, T. & SMITH, A. M. O. 1974 *Analysis of Turbulent Boundary Layers.* Academic.

CHORIN, A. J. & BERNARD, P. S. 1972 Discretization of a vortex sheet, with an example of roll-up. *Univ. Calif. Rep.* FM-72-5.

CLEMENTS, R. R. 1977 Flow representation, including separated regions, using discrete vortices. *VKI Lecture Series, Computational fluid mechanics, Rhode-Saint-Genèse, Belgium.*

CORINO, E. R. & BRODKEY, R. S. 1969 A visual investigation in the wall region of turbulent flow. *J. Fluid Mech.* **37**, 1.

DINCKELAKKER, A., HESSEL, M., MEIER, G. E. A. & SCHEWE, G. 1977 Investigation of pressure fluctuations beneath a turbulent boundary layer by means of an optical method. *Phys. Fluids* **20**, S216.

ECKELMANN, H. 1974 The structure of the viscous sublayer and the adjacent wall region in a turbulent channel flow. *J. Fluid Mech.* **65**, 439.

EINSTEIN, H. A. & LI, H. 1956 The viscous sublayer along a smooth boundary. *Proc. A.S.C.E. J. Engng Mech. Div.* **82** (EM2), 945.

FALCO, R. E. 1977 Coherent motion in the outer region of turbulent boundary layers. *Phys. Fluids Suppl.* **20**, 124.

FAVRE, A., GAVIGLIO, J. & DUMAS, R. 1967 Structure of velocity space–time correlations in a boundary layer. *Phys. Fluids Suppl.* **10**, 138.

FENDELL, F. E. 1972 Singular perturbation and turbulent shear flow near walls. *J. Astronautical Soc.* **20**, 129.

GUPTA, A. K., LAUFER, J. & KAPLAN, R. E. 1971 Spatial structure in the viscous sublayer. *J. Fluid Mech.* **50**, 493.

HANRATTY, T. J. 1956 Turbulent exchange of mass and momentum with a boundary. *A.I.Ch.E. J.* **2**, 359.

HEAD, M. R. & BANDYOPADHYAY, P. 1979 Flow visualization of turbulent boundary layer structure. AGARD Symp. on Turb., The Hague.

HINZE, J. O. 1975 *Turbulence*, 2nd edn. McGraw-Hill.

KIM, H. T., KLINE, S. J. & REYNOLDS, W. C. 1971 The production of turbulence near a smooth wall in a turbulent boundary layer. *J. Fluid Mech.* **50**, 133.

KLINE, S. J., REYNOLDS, W. C., SCHRAUB, F. A. & RUNDSTADLER, P. W. 1967 The structure of turbulent boundary layers. *J. Fluid Mech.* **30**, 741.

KOVASZNAY, L. S. G., KIBENS, V. & BLACKWELDER, R. F. 1970 Large-scale motion in the intermittent region of a turbulent boundary layer. *J. Fluid Mech.* **41**, 283.

LAMB, H. 1932 *Hydrodynamics*, 6th edn. Cambridge University Press.

LANDAHL, M. T. 1965 A wave-guide model for turbulent shear flow. *N.A.S.A.* CR-317.

LANDAHL, M. T. 1967 A wave-guide model for turbulent shear flow. *J. Fluid Mech.* **29**, 441.

LANDAHL, M. T. 1975 Wave breakdown and turbulence. *SIAM J. Appl. Mech.* **28**, 735.

LAUFER, J. 1972 Recent developments in turbulent boundary layer research. *Inst. Naz. Alta. Mat., Symp. Math.* **9**, 299.

LAUFER, J. & BADRI NARAYANAN, M. A. 1971 The mean period of the production mechanism in a boundary layer. *Phys. Fluids* **14**, 182.

MAGER, A. 1964 Three-dimensional laminar boundary layers. In *Theory of Laminar Flows* (ed. F. K. Moore). Princeton University Press.

MELLOR, G. L. 1972 The large Reynolds number asymptotic theory of turbulent boundary layers. *Int. J. Engng Sci.* **10**, 851.

NYCHAS, S. G., HERSHEY, H. C. & BRODKEY, R. S. 1973 A visual study of turbulent shear flow. *J. Fluid Mech.* **61**, 513.

OFFEN, G. R. & KLINE, S. J. 1974 Combined dye-streak and hydrogen bubble visual observations of a turbulent boundary layers. *J. Fluid Mech.* **62**, 223.

OFFEN, G. R. & KLINE, S. J. 1975 A proposed model of the bursting process in turbulent boundary layers. *J. Fluid Mech.* **70**, 209.

OOMS, G., GROEN, G., DE GRAAG, D. P. & BALLINTIJN, J. F. 1978 On turbulent pipe flow with heat transfer and chemical reaction. *6th Int. Heat Transfer Conf., Toronto*, paper FC(b)-35.

PRATURI, A. K. & BRODKEY, R. S. 1978 A stereoscopic visual study of coherent structures in turbulent shear flow. *J. Fluid Mech.* **89**, 251.

RAO, K. N., NARASIMHA, R. & BADRI NARAYANAN, M. A. 1971 The bursting phenomenon in a turbulent boundary layer. *J. Fluid Mech.* **48**, 339.

SCHUBERT, G. & CORCOS, G. M. 1967 The dynamics of turbulence near a wall according to a linear model. *J. Fluid Mech.* **29**, 113.

SHEN, S. F. 1964 Stability of laminar flows. In *Theory of Laminar Flows* (ed. F. K. Moore). Princeton University Press.

STERNBERG, J. 1962 A theory for the viscous sublayer of a turbulent flow. *J. Fluid Mech.* **13**, 241.

STUART, J. T. 1965 The production of intense shear layers by vortex stretching and convection. *AGARD Rep.* 514.

TENNEKES, H. 1968 Outline of a second-order theory for turbulent pipe flow. *A.I.A.A. J.* **6**, 1735.

THOMAS, L. C., CHUNG, B. T. F. & MAHALDAR, S. K. 1971 Temperature profiles for turbulent flow of high Prandtl number fluids. *Int. J. Heat Mass Transfer* **14**, 1465.

TOWNSEND, A. A. 1961 Equilibrium layers and wall turbulence. *J. Fluid Mech.* **11**, 97.

TOWNSEND, A. A. 1976 *The Structure of Turbulent Shear Flow*, 2nd edn. Cambridge University Press.

UEDA, H. & HINZE, J. O. 1975 Fine structure turbulence in the wall region of a turbulent boundary layer. *J. Fluid Mech.* **67**, 125.

VAN DONGEN, F. G., BELJAARS, A. C. M. & DE VRIES, D. A. 1978 A periodic and intermittent model for the wall region of a turbulent boundary layer. *Int. J. Heat Mass Transfer* **21**, 1099.

VAN DYKE, M. 1975 *Perturbation Methods in Fluid Mechanics*. Stanford, California: Parabolic.

WILLMARTH, W. W. 1975*a* Structure of turbulence in boundary layers. *Adv. Appl. Mech.* **15**, 159.

WILLMARTH, W. W. 1975*b* Pressure fluctuations beneath turbulent boundary layers. *Ann. Rev. Fluid Mech.* **7**, 13.

WILLMARTH, W. W. & WOOLDRIDGE, C. E. 1962 Measurements of the fluctuating pressure at the wall beneath a thick turbulent boundary layer. *J. Fluid Mech.* **14**, 187.

WILLS, J. A. B. 1971 Measurements of the wave-number/phase velocity spectrum of wall pressure beneath a turbulent boundary layer. *J. Fluid Mech.* **45**, 65.

WITTING, H. 1958 Über den Einfluss der Strömlinienkrümmung auf die Stabilität laminarer Strömungen. *Arch. Rat. Mech. Anal.* **2**, 243.